Cancer Letters 567 (2023) 216262

Contents lists available at ScienceDirect

Cancer Letters

journal homepage: www.elsevier.com/locate/canlet

The NF–Y splicing signature controls hybrid EMT and ECM-related pathways to promote aggressiveness of colon cancer

Giovanna Rigillo [a,1,2], Silvia Belluti [a,2], Virginia Campani [a,2], Gregorio Ragazzini [d], Mirko Ronzio [b], Giacomo Miserocchi [c], Beatrice Bighi [d], Laura Cuoghi [a], Valentina Mularoni [a], Vincenzo Zappavigna [a], Diletta Dolfini [b], Laura Mercatali [c], Andrea Alessandrini [d,e], Carol Imbriano [a,*]

[a] Department of Life Sciences, University of Modena and Reggio Emilia, via Campi 213/D, 41125, Modena, Italy
[b] Department of Biosciences, University of Milan, via Celoria 26, 20133, Milan, Italy
[c] Preclinic and Osteoncology Unit, Biosciences Laboratory, IRCCS Istituto Romagnolo per lo Studio dei Tumori (IRST) "Dino Amadori", 47014, Meldola, Italy
[d] Department of Physics, Informatics and Mathematics, University of Modena and Reggio Emilia, via Campi 213/A, 41125, Modena, Italy
[e] CNR-Nanoscience Institute-S3, Modena, Italy

ARTICLE INFO

Keywords:
NF-Y
Alternative splicing
CCAAT
Colon cancer
Cell migration
Metastasis
EMT
ECM
E-Cadherin

ABSTRACT

Aberrant splicing events are associated with colorectal cancer (CRC) and provide new opportunities for tumor diagnosis and treatment. The expression of the splice variants of NF-YA, the DNA binding subunit of the transcription factor NF–Y, is deregulated in multiple cancer types compared to healthy tissues. NF–YAs and NF–YAl isoforms differ in the transactivation domain, which may result in distinct transcriptional programs. In this study, we demonstrated that the NF–YAl transcript is higher in aggressive mesenchymal CRCs and predicts shorter patients' survival. In 2D and 3D conditions, CRC cells overexpressing NF–YAl (NF-YAl^{high}) exhibit reduced cell proliferation, rapid single cell amoeboid-like migration, and form irregular spheroids with poor cell-to-cell adhesion. Compared to NF-YAs^{high}, NF-YAl^{high} cells show changes in the transcription of genes involved in epithelial-mesenchymal transition, extracellular matrix and cell adhesion. NF–YAl and NF–YAs bind similarly to the promoter of the E-cadherin gene, but oppositely regulate its transcription. The increased metastatic potential of NF-YAl^{high} cells *in vivo* was confirmed in zebrafish xenografts.

These results suggest that the NF–YAl splice variant could be a new CRC prognostic factor and that splice-switching strategies may reduce metastatic CRC progression.

1. Introduction

NF–Y is a heterotrimeric transcription factor, composed by the DNA binding subunit NF-YA and the histone-fold domain NF-YB/NF-YC dimer [1]. Multiple bioinformatic studies demonstrated that the NF–Y binding site, the CCAAT box, is one of the most represented promoter elements in eukaryotic cells [2–5]. In particular, the CCAAT box is among transcription factor binding sites (TFBS) identified in the regulatory regions of tumor-associated genes (reviewed in Ref. [6]). Consistently, NF–Y activates genes of cellular pathways commonly altered in cancer cells, such as cell cycle and metabolic ones [4,7]. Transcription levels of NF–Y subunits are altered in cancer tissues and cells: NF-YA is up-regulated in different tumors, such as gastric, lung, breast, ovarian, osteosarcoma and prostate cancers [8–14], while NF-YC increase has been described in glioma and choroid plexus carcinomas (CPC) [15,16].

In the last years, much attention has been given to alternative splicing regulation of NF–Y, in particular NF-YA. The NF-YA gene encodes for two splice variants, NF–YAs and NF–YAl, with the last one including additional 28/29 amino acids stretch (exon 3) within the transactivation domain. The two NF-YA proteins can modulate different transcriptional programs, with even opposite effects on cell proliferation and differentiation processes [17]. In the endometrium, NF–YAl is exclusively expressed in benign tissues, while NF–YAs is observed in

* Corresponding author.
E-mail addresses: cimbriano@unimo.it, carol.imbriano@unimore.it (C. Imbriano).
[1] Present address: Department of Biomedical, Metabolic and Neural Sciences, University of Modena and Reggio Emilia, via Campi 287, 41125 Modena, Italy.
[2] These authors contributed equally.

https://doi.org/10.1016/j.canlet.2023.216262
Received 31 March 2023; Received in revised form 24 May 2023; Accepted 4 June 2023
Available online 10 June 2023

cancer and poorly differentiated ones [6,18]. NF–YAs increases at the expense of NF–YAl in lung adenocarcinoma (LUAD), lung squamous cell carcinoma (LUSC), breast (BRCA) and prostate (PCA) cancers [10] Despite this, data from LUSC, BRCA and PCA clearly showed that a decrease in NF–YAs/NF–YAl ratio is linked to a pro-migration signature and an aggressive metastasis-prone phenotype, characterized by the loss of epithelial and acquisition of epithelial-mesenchymal transition (EMT) features [13].

Colorectal cancer (CRC) is the third most commonly diagnosed tumor cancer in men and the second in women worldwide. In particular, colon adenocarcinoma (COAD) is the most prevalent type of CRC. The Tumor, Node, Metastases (TNM) staging is currently used to predict the prognosis for CRC affected patients, it guides the need for adjuvant therapy after potentially curative surgery and allows to select patients for participation in clinical trials [19].

On the basis of multiple sets of data, including DNA copy number and DNA methylation, messenger RNA (mRNA) and microRNA (miRNA) expression, and exome sequencing, three major molecular subtypes have been identified: MSI/CIMP (microsatellite instability/epigenomic CpG island methylator phenotype), CIN (chromosomal instability) and invasive subtypes [20].

In addition to gene expression-based subtyping, CRC gene expression heterogeneity is best described through four internationally approved Consensus Molecular Subtypes (CMS) [21]. The CMS1 group is characterized by hypermutation, enrichment of BRAF mutation and immune infiltration, while the canonical epithelial subtype CMS2 shows strong upregulation of WNT and MYC; KRAS-metabolic adaptation distinguishes the metabolic subtype CMS3, and the stemness, EMT and extra cellular matrix (ECM)-remodeling transcriptional signature characterizes the mesenchymal subtype CMS4.

The ECM is a key component of the tumor microenvironment and contributes to cancer pathogenesis by modulating immune response, proliferation and survival of tumor cells, and cancer cell migration [22,23].

With the aim to identify a possible NF-YA splicing signature for stratification of CRC patients, we found a significant association between a reduced NF–YAs/NF–YAl ratio and those CRC subtypes characterized by ECM transcriptional profiles, such as MSI/CIMP and CMS4 subtypes. Through the modulation of NF-YA isoforms, we demonstrated that NF–YAl overexpression impairs cell proliferation, anchorage-dependent and -independent cell growth. High NF–YAl levels trigger a pro-migratory behavior of CRC cells both in 2D and 3D culture conditions. Time-lapse imaging highlighted that NF–YAl enhances fast single cell amoeboid-like migration, in opposition to NF–YAs that promotes collective migration. NF-YAl^{high} cells are characterized by a transcriptional signature associated with ECM and EMT. The two NF-YA isoforms control the expression of E-cadherin through direct binding to its CCAAT-promoter region, with NF–YAs activating and NF–YAl inhibiting E-cadherin transcription. Further, we investigated the different aggressiveness of CRC cells *in vivo*: compared to NF-YAs^{high}, NF-YAl^{high} cells showed greater metastatic potential when injected into transgenic zebrafish, a model for metastasis extravasation.

Altogether, our data clearly suggest that the two NF-YA variants can be key markers for CRC patients stratification, with high NF–YAl expression being a hallmark of cancer cell dissemination and CMS4 mesenchymal subtype.

2. Materials and methods

2.1. TCGA data analysis

RNA-seq raw counts data of TCGA COAD cohort were retrieved from firebrowse (http://firebrowse.org/) webpage. The dataset is composed of 500 samples, 41 of which normal tissues and 459 tumor tissues. Clinical and survival data were downloaded from UCSC Xena repository [24]. Genes and isoforms raw counts were normalized using DESeq2 R package [25].

Survival analyses according to expression data were performed stratifying the patients for which the Progression Free Interval (PFI) information was available in two groups: one including the first three quartiles (high) and the other one comprising the last quartile (low). Significant differences in survival were assessed according to the Kaplan–Meier analysis and log-rank test.

Comparisons of NF–Y subunits or NF-YA isoforms between conditions were conducted on normalized counts and statistical significance was assessed with Wilcoxon rank-sum test. NF–YAs/NF–YAl ratio was computed as the Log2 of normalized counts ratio after the addition of a pseudovalue equal to 1. All bioinformatic analyses were performed in the R programming environment (version 4.2.0) using the ggplot2, ggpubr, survival, survminer, tidyverse packages.

2.2. TCGA samples classification

Expression subtype of TCGA samples was assigned using the deep learning-based framework DeepCC [26], employing as training set 220 samples classified in mRNA clusters [20]. Analogously, the samples were classified into Consensus Molecular Subtypes using as training set the 371 labeled TCGA samples available [21].

2.3. CRC cell lines RNA-seq data processing

Raw RNA-seq data of Cancer Cell Line Encyclopedia (CCLE) were retrieved on Sequence Read Archive (SRA). Reads were aligned to human transcriptome with bowtie2 [27] and transcripts were quantified with RSEM v. 1.3.1 [28].

2.4. Promoter analysis

In silico analysis of promoter sequences (−950 to +50 relative to transcription start site) for the presence of putative NF–Y binding sites was performed with the computational algorithm Lasagna-Search 2.0 (https://biogrid-lasagna.engr.uconn.edu/lasagna_search/), with TRANSFAC and JASPAR core matrices for NF–Y and NFYA, using default system parameters and cutoff p-value of 0.001. We assessed the presence of the CCAAT/ATTGG pentanucleotide by manual inspection of each promoter in the UCSC Genome Browser (http://genome.ucsc.edu) through the Short Match Track Settings, and the presence of NF–Y binding from the ENCODE Project, through the Transcription Factor ChIP-seq Peaks from ENCODE 3 tracks in the UCSC Genome Browser (human GRCh37/hg19).

2.5. Cell lines, treatments and lentiviral transduction

HT29 (ATCC Cat# HTB-38), RKO (ATCC Cat# CRL-2577) and HFF (ATCC Cat# SCRC-1041) cells were grown in DMEM High Glucose Medium (Biowest, France). HCT116 (ATCC Cat# CCL-247) were grown in IMDM Medium (Biowest, France). All media were supplemented with 2 mM glutamine, 100 IU/ml penicillin, 100 μg/ml streptomycin and 10% FBS (Gibco). The cells were grown at 37 °C and 5% CO_2 with saturating humidity.

Stable NF-YA-overexpressing cell lines were obtained by lentiviral infection of HCT116 and HT29 cells with pSIN–NF–YAs, pSIN–NF–YAl or control pSIN-empty particles for 48 h [41]. Infected cells were then selected using puromycin (3 μg/ml) and maintained in medium supplemented with puromycin (0,8 μg/ml), as previously described [14].

For protein degradation inhibition assay, HCT116 cells (3×10^5/well) were grown in complete medium for 24 h, then treated with 10 μM Chloroquine (Sigma Aldrich) and 50 μM Z-Leu-Leu-Leu-H (MG132; AbMole Bioscience) for 16 h.

2.6. Anchorage-independent and anchorage-dependent 3D colony assay

For anchorage-independent colony formation assay, 0.6% low melt agarose gel with 10% FBS in appropriate complete cell growth medium was prepared and added to 6-well plate as a base agar. 5×10^3 cells/well were resuspended in 0.22% (HCT116) or 0.3% (HT29) agarose gel in appropriate complete cell growth medium and plated on top of a base layer. After 3 weeks (HCT116) or 2 weeks (HT29) colonies were stained with 0.07% crystal violet solution in 1X PBS. Plates were imaged and colonies were counted in three independent experiments.

The xeno-free hydrogel system (Vitrogel 3D, TheWell Bioscience,NJ) that mimics the natural ECM environment was used for anchorage-dependent colony formation assay from single cell. After warming, Vitrogel 3D was diluted with 0.1X PBS (1:1), and then gently mixed with HCT116 cells suspension (5×10^3/well) (2:1). 75 μl of hydrogel/cell mixture were transferred into a 96-well plate and, after 15 min of incubation for stabilization, 75 μl of complete IMDM medium was added to the hydrogel into each well. Cell growth and cluster formation were imaged after 1 week by EVOS M5000 microscope (Thermo Fisher Scientific, MA).

2.7. Cell proliferation assay

5×10^3 HCT116 or HT29 overexpressing cells were seeded into 96-well plate and grown in complete medium. After 24 h, 48 h, 72 h, 96 h, PrestoBlue reagent (#A13261, Thermo Fisher Scientific, MA) was added to the medium (1:9 v/v) and incubated for 1 h at 37 °C. Cell viability was calculated by quantifying PrestoBlue reduction by measuring the absorbance at 570–620 nm, according to the manufacturer's protocol. Three independent experiments were performed.

2.8. Migration and invasion assays

Cell motility was studied in Transwell membranes (pore size 8 μm; #3464, Corning), as previously described [14]. HCT116 overexpressing cells were starved overnight and 5×10^5 cells were seeded in 100 μl of serum free medium into the upper chamber of the Transwell. Complete IMDM medium containing 10% FBS was used as chemoattractant in the lower chamber. After 96 h, the cells were removed from the upper chambers with a cotton swab, while cells on the underside of the inserts were fixed and stained with 0.5% crystal violet solution in 20% Methanol, for 15 min. Inserts were then washed with distilled water, dried and imaged with an EVOS M5000 microscope (Thermo Fisher Scientific, MA). Cells were counted in five randomly selected fields of each sample and percent migration was calculated, according to the manufacturer's protocol.

Cell migration was further studied in Alvetex scaffolds (12-well insert, #AVP005, Reprocell, UK): the membranes were hydrated in 70% ethanol and washed in culture medium. 5×10^5 HCT116 overexpressing cells were dispensed in 75 μl of medium on the middle of the disc, and incubated for 2 h at 37 °C to facilitate cell attachment, then the wells were filled with complete growth medium below and above the membrane. After 72 h, Alvetex scaffolds were washed with 1X PBS, embedded in OCT matrix and processed for cryosectioning. Longitudinal sections of 10 μm were stained with standard haematoxylin and eosin (H&E) or processed for immunofluorescence. Images were obtained with an EVOS M5000 microscope (Thermo Fisher Scientific, MA) and the percentage of cell penetration was measured with ImageJ software.

Wound healing cell migration assay: HCT116 or HT29 overexpressing cells (6×10^4) were seeded into Ibidi culture-insert (#80209, Ibidi GmbH, Germany) and cultured until confluence, then the insert was removed to create the gap. The cells were gently washed with 1X PBS and complete IMDM medium was provided. Images were acquired with an EVOS M5000 microscope (Thermo Fisher Scientific, MA) immediately after insert removal (T0) and up to 48 h for HCT116 and 72 h for HT29 cells. Wound areas were measured by using Photoshop software and residual wound area (%) was calculated with the formula: final area/initial area × 100.

Wound healing co-culture assay: HFF (6×10^4) and HCT116-overexpressing (6×10^4) cells were seeded into two adjacent wells of the same *Ibidi* culture-insert and cultured until confluence was reached. Before removing the insert, HCT116 and HFF were stained with Vibrant DiO Cell-Labeling solution (#V22886, Molecular Probes) or DAPI for 10 min, respectively. The insert was removed to create the gap, the cells were gently washed with 1X PBS and complete medium was provided. Images were acquired with an EVOS M5000 microscope (Thermo Fisher Scientific, MA) immediately after insert removal (T0) and up to 72 h.

2.9. Immunofluorescence

Alvetex sections were fixed for 20 min with 10% Formalin Solution (#HT5014, Merck KGaA), rinsed three times with 1X PBS for 5 min and permeabilized with ice-cold 1X PBS/0.5% TritonX-100 for 10 min at RT. Sections were incubated 1 h in blocking buffer (4% BSA, 0.1% TritonX-100 in 1X PBS) and then incubated over-night at 4 °C with rabbit anti-Ki-67 antibody (dilution 1:300 in blocking buffer; #9129, Cell Signaling). After two washes with 1X PBS for 5 min, Alexa-fluor 488-conjugated antibody (dilution 1:400 in blocking buffer; #A-21206, Thermo Fisher Scientific, MA) was incubated for 1 h at RT, followed by nuclei staining with DAPI (1:5000 in 1X PBS) for 10 min. After washing with 1X PBS, sections were mounted on slides with imaging spacers in Mowiol. Images were acquired using an EVOS M5000 (Thermo Fisher Scientific, MA) fluorescence microscope.

For E-cadherin immunofluorescence, HCT116 cells were seeded on coverslips and grown to confluence. Cells were fixed for 15 min in 10% Formalin Solution (#HT5014, Merck KGaA), rinsed twice in 1X PBS and permeabilized with ice-cold 1X PBS/0.05% TritonX-100 for 10 min at RT. After incubation in blocking buffer (1% BSA in 1X PBS) for 30 min, samples were first incubated overnight at 4 °C with anti-E-cadherin antibody (dilution 1:1000 in in blocking buffer; #3195, Cell Signaling), then for 1 h with anti-rabbit Alexa-fluor 488-conjugated antibody (dilution 1:400 in blocking buffer; #A-21206, Thermo Fisher Scientific). Nuclei were counterstained with DAPI. After washing with 1X PBS, the cells were mounted on slides in Mowiol. Images were obtained using an EVOS M5000 (Thermo Fisher Scientific) fluorescence microscope.

2.10. 3D multicellular tumor spheroids (MTSs)

5×10^3 HCT116 overexpressing cells were plated into 96-well Round Bottom Ultra-Low Attachment (ULA) plates (#7007 and #4515, Corning, USA) in 150 μl complete ice-cold medium containing 1 mg/ml Matrigel matrix (#354248, Corning, USA) followed by centrifugation for 10 min at 1000×*g*, 4 °C, using no braking. MTSs were incubated for 7 days at 37 °C and 5% CO_2 in humidified incubator. 50 μL of fresh complete medium was added every 3 days. MTSs images were acquired with an EVOS M5000 microscope (Thermo Fisher Scientific, MA) [14].

To assess cell dissemination from spheroids, MTSs were gently collected after four days of culture and washed with 1X PBS, using cut P200/P1000 pipette tips to preserve morphology, then one 50 μl drop containing one MTS was transferred into a 96-well flat bottom plate and submerged in culture medium. MTS-detached cells were monitored up to 6 days by EVOS M5000 imaging system (Thermo Fisher Scientific, MA).

Spheroid 3D cells invasion was assessed by transferring MTSs on a collagen-based substrate. The collagen matrix was prepared as follows: high-concentrated rat tail collagen I (#7341085, Corning, USA) (3 mg/ml) was mixed with NaOH, NaHCO3 and IMDM medium, in ice-cold condition. After controlling pH (7–8), 100 μL of matrix were dispensed into 96-well plate and allowed to polymerize for 30 min at 37 °C. MTSs were gently collected and washed with 1X PBS, using cut P200/P1000 pipette tips to preserve morphology, then one 50 μl drop

containing one MTS was transferred on the collagen layer and complete IMDM medium was provided. Spheroid cell invasion was monitored and imaged up to 7 days by EVOS M5000 imaging system (Thermo Fisher Scientific, MA).

2.11. Time-lapse imaging

Time-lapse imaging was performed using a home-developed on-stage cell incubator [29]. The system provides an environment at constant temperature of 37 °C and constant 5% CO_2 concentration. For wound healing experiments, live cell imaging was performed with an Olympus IX 70 microscope equipped with a 20X phase-contrast objective (NA 0.75) and a CMOS camera (Hamamatsu ORCA-flash 4.0LT - C11440). The live-cell imaging incubator was mounted on a home-developed motorized x–y stage to acquire images at multiple positions (up to 12) with an auto-focus system developed exploiting a stepper-motor connected to the objective lens knob and controlled by Arduino Uno and a purposely written Python software. For each sample, a mosaic of 2 × 2 adjacent images was acquired and a stitching of the images was the performed using the Fiji built-in plugin Grid Stitching (https://imagej.net/plugins/grid-collection-stitching) [30]. In the case of live-imaging of the multicellular spheroids, a 10x bright field objective was used. Images were acquired every 6 or 8 min for a total time up to 48 h.

2.12. Wound healing image analysis

The profile of the advancing cell-sheet edges in wound-healing experiments was measured by a specifically developed Fiji macro and a Python software. Briefly, adjacent images acquired during live-cell imaging were fused in 2 × 2 mosaics by using the Fiji built-in plugin *Grid Stitching*. Such mosaics were aligned in a time-lapse sequence with a second built-in plugin, *Template Matching/Align slices in stack*. Afterwards, in order to establish the perimeter of the closing wound and the complexity of the advancing cell front, an already existing macro *Wound_healing_size_tool* [31] was modified to best suit our requirements. The macro, as originally conceived by the authors, allows to contour the cell front with customizable parameters and quantify the wound area; we included a function that enables the export of the x-y coordinates of the contour points in a text file. Finally, a dedicated script in Python was developed to extrapolate the x-y coordinates of the two facing cell fronts, to discard outliers defects as well as floating cells not included in the cell-sheets and add missing points. The obtained effective length of the cell-sheet edge was then divided by the acquired image width to obtain a parameter expressing the complexity of the advancing front, defined as follows (L/D):

$$L \Big/ D = \frac{Front_{Length}}{Image_{Width}} = \frac{\sum_{i=0}^{i=N-1} \sqrt{(x_i - x_{i+1})^2 + (y_i - y_{i+1})^2}}{Image_{Width}}$$

This parameter (by definition always >1) allows to distinguish the characteristics of the different cell populations between a more individual or collective migration propensity. In the case of more individual migration, the complexity parameter is higher than that obtained in the second case. The script also traces the mean position of the points of both left and right fronts over time, in order to measure the mean front displacement with respect to the initial mean position.

PIV (Particle Image Velocimetry) analysis was performed by the Open PIV MATLAB software. This analysis allows to extract the velocity trend in snapshots of the same sample area obtained at different times. In the plots we reported the magnitude of the speed with a false color scale and we overlaid arrows to indicate the directionality of the speed. For the analysis, we used averages over time in a time interval of about 30 min. From the x and y components, we calculated the angle of the velocity with respect to the perpendicular to the cell sheet edge.

2.13. Protein extraction and immunoblotting

Whole-cell protein extracts were prepared by lysis of 2D cultured cells into 1X SDS sample buffer (25 mM Tris–HCl pH 6.8, 1.5 mM EDTA, 20% glycerol, 2% SDS, 5% β-mercaptoethanol, 0.0025% Bromophenol blue). Protein lysates of MTSs were obtained from a pool of at least eight spheroids. After two washes with 1X PBS, MTSs were disaggregated with 0,1% trypsin for 10 min at 37 °C, then resuspended in medium and centrifuged at 3000 rpm for 5 min. Cell pellets were washed with 1X PBS and lysed in 1X SDS sample buffer. Equivalent amounts of cellular extracts were resolved by SDS-PAGE, transferred to nitrocellulose membrane (GE Healthcare) with Trans-Blot Turbo Transfer System (Bio-Rad, USA) and immunoblotted with the following primary antibodies, diluted 1:1000 in 1X TBS with 1 mg/ml BSA: rabbit anti-vimentin (#D21H3 XP, Cell Signaling), rabbit anti-Snail (#C15D3, Cell Signaling), rabbit anti-Slug (#C19G7, Cell Signalling), rabbit anti-E-cadherin (#3195, Cell Signaling), mouse anti–NF–YA (G2) (#sc-17753, Santa Cruz Biotechnology), rabbit anti-AKT (#MAB2055, R&D Systems), rabbit anti-phospho-AKT(S473) (#AF887, R&D Systems), rabbit anti-RhoA (67B9, #9968, Cell Signaling),rabbit anti-RhoC (D40E4, #9968, Cell Signaling),mouse anti-Tubulin (#66031, Proteintech Europe). Membranes were blotted and scanned with Amersham Imager AI680 RGB (GE Healthcare), using chemiluminescent detection reagents Westar ηC and Supernova HRP substrates (Cyanagen).

2.14. RNA extraction and RT-qPCR

RNA was extracted from cells by using Ripospin II mini Kit (#314–150, GeneAll), according to the manufacturer's protocol. For cDNA synthesis, 200 ng of RNA was retrotranscribed with PrimeScript RT Reagent Kit (#RR037A, Takara Bio). Quantitative RealTime PCR was performed with SsoAdvanced Universal SYBR Green Supermix (#1725274, Bio-Rad, USA) using Biorad CFX connect Real-Time PCR Detection System. Oligonucleotides sequences are listed in Supplementary Table 1. Data were analyzed using the Bio-Rad CFX Maestro 2.0 software (Bio-Rad) and mRNA expression was normalized to Rps20. For transcriptomic analysis of "Extracellular matrix and adhesion molecules", 20 ng/μL of cDNA were loaded into predesigned 96-well plate panel (#10034145, Bio-Rad, USA) and quantitative RealTime PCR was performed by using Roche LC480 thermocycler with SsoAdvanced Universal SYBR Green Supermix.

2.15. Chromatin immunoprecipitation

Chromatin was prepared from subconfluent HCT116 cells and ChIP was performed as previously described [32,33]. Each IP was incubated overnight at 4 °C on a rotating wheel with the following antibodies: 1 μl of anti–NF–YA (#C15310261, Diagenode), 4 μg of anti–NF–YB (Pab001, GeneSpin) or rabbit IgG (sc-2027, Santa Cruz Biotechnology). Immunoprecipitated DNAs were isolated by phenol-chloroform extraction and resuspended in Tris-EDTA buffer. Quantitative Real-Time PCR was performed with SsoAdvanced Universal SYBR Green Supermix (#1725274, Bio-Rad) in the Bio-Rad CFX connect machine. Sequences of primers used are listed in Supplementary Table 2.

2.16. Cell transfection and luciferase assay

Sub-confluent HCT116 overexpressing cells were transfected in 24-well plates using Lipofectamine 2000 Transfection Reagent (Invitrogen), according to the protocol provided by the manufacturer. Cells were recovered 24 h after transfection and resuspended in lysis buffer (1% TritonX 100, 25 mM GlyGly pH 7.8, 15 mM MgSO4, 4 mM EGTA pH 8). Luciferase activity was measured on a GloMax Discover microplate reader (Promega). 250 ng of the Cdh1 promoter luciferase construct (proE-cad178-Luc, Addgene plasmid # 42081 [34]) were co-transfected with 100 ng of pCMV GFP and 100-200-300 ng of pSG5-NF-YA-DN

vector encoding for the NF-YA dominant negative mutant or pSG5 expression vector encoding for murine NF–YAl and NF–YAs [35,36]. The results were normalized to protein concentration (Bradford reagent, Sigma Aldrich) and percentage of GFP-positive cells, measured by Attune NxT Flow Cytometer (Thermo Fisher Scientific). Four independent transfections were performed.

2.17. Zebrafish injection of cancer cells

Fertilized eggs from the Tg(fli1:EGFP) transgenic zebrafish strain were obtained from natural spawning, maintained in fish water with 0.1% of Methylene Blue and raised at 28 °C, according to Kimmel et al. [37]. Before handling, larvae were anesthetized in 0.02% tricaine solution (Sigma-Aldrich).

Prior to injection, cancer cells were collected by trypsinization and labeled with red (CellTracker™ CM-DiI, Invitrogen) or deep red fluorescent dye (CellTracker™ Deep Red, Invitrogen) for 20–30 min and resuspended in PBS at a concentration of 2.5 × 105/μL. Tg(fli1:EGFP) transgenic zebrafish embryos were dechorionated at 48 h post-fertilization (hpf), anesthetized before injection and oriented in a lateral orientation on an agarose bed. 300/500 cells were implanted in the sub-peridermal space of larvae using a pulled micropipette. Embryos injected in the perivitelline space that show cancer cells in circulation were excluded. The selected embryos were incubated at 34 °C. At 24 h post-injection (hpi), the presence of circulating cells was evaluated using a confocal microscope (Nikon Corporation, Tokyo, Japan) and images analyzed with the NIS Elements software (Nikon Corporation, Tokyo, Japan).

2.18. Statistical analysis

Data represent the mean of at least three independent experiments ± standard deviation. Statistical analyses were performed using GraphPad PRISM 8.0 software using one-way ANOVA or unpaired Student's t-test, as appropriate. p values < 0.05 were considered to be statistically significant: (*), $p < 0.01$ (**), $p < 0.001$ (***), and $p < 0.0001$ (****).

3. Results

3.1. The expression of NF-YA transcript variants is deregulated in CRC patients

To investigate the possible role of NF–Y in colon cancer, we first analyzed the expression levels of NF–Y subunits in COAD (colon adenocarcinoma) patients. TCGA data clearly showed a significant overexpression of both NF-YA and NF-YB transcripts, in opposition to NF-YC that was down-regulated in tumor compared to normal samples (Fig. 1A). The increase in NF-YA transcripts is ascribable to the NF–YAs variant, which is up-regulated in opposition to NF–YAl (Fig. 1B), as already observed for other types of cancers [9,10,14,38]. We then evaluated the ratio between NF–YAs and NF–YAl transcripts in patients stratified according to lymph node involvement, a determining prognostic classification used for therapeutic decisions: NF–YAl significantly increases in patients characterized by a high number of positive lymph nodes (n = 11–16 and n = 17+ categories) versus negative patients (n = 0) (Fig. 1C, left panel). Despite not statistically significant, the increase in NF–YAl levels was paralleled by a decreasing trend in the NF–YAs/NF–YAl ratio (Fig. 1C, right panel). While total NF-YA or NF–YAs levels did not correlate with the overall survival probability of patients (OS) (Suppl. Fig. 1A and B), we observed a significant reduction in OS in patients characterized by high NF–YAl mRNA compared to those with low transcript levels (Fig. 1D).

To further explore the hypothesis that NF–YAl could discriminate aggressive CRC, we analyzed the expression of NF-YA isoforms in CRC patients stratified on the basis of CMS subtypes (Fig. 1E). Compared to normal samples, NF–YAs increases in all CMS subtypes with the exception of CMS1, while NF–YAl decreases in all CMSs, CMS4 excluded. Hence, with respect to other CMS tumor subtypes, a lower NF–YAs/NF–YAl ratio is observed in CMS4, which is characterized by a mesenchymal subtype that involves the upregulation of EMT pathways, TGF-β signaling, matrix remodeling, stromal infiltration, poor relapse-free and survival (Suppl. Fig. 1C) [21]. Similarly, we identified a significant upregulation of NF–YAl transcription in the MSI/CIMP group, which is enriched for the CMS4 subtype (Suppl. Fig. 1C and D). Interestingly, the CMS2 cluster showed an increase in the NF–YAs transcript compared to the other CMS subtypes, consistently with the key role of NF–YAs in proliferation and cell cycle pathways, gene sets that are enriched in CMS2 adenomas (Fig. 1E) [13,17,21,39].

These results suggest that higher NF-YAI expression could predict increased CRC aggressiveness and metastasis, presumably through the acquisition of a migratory/EMT phenotype, as observed in the CSM4 group.

3.2. High NF–YAl levels correlate with the expression of mesenchymal markers and enhance cell migration

To determine whether the two NF-YA isoforms can differently sharpen CRC behavior, we decided to use *in vitro* cellular models. By Western blot, we analyzed the protein levels of NF–YAs and NF–YAl in three different CRC cell lines: the epithelial HT29 cells, which have intermediate capacity to differentiate, the aggressive non-differentiating HCT116 cell line, and the mesenchymal RKO cells (Fig. 2A). The levels of the EMT markers Vimentin, Snail and Slug confirmed the epithelial, epithelial/mesenchymal, and mesenchymal phenotypes of HT29, HCT116 and RKO cells, respectively. Although NF–YAs is the predominant isoform in all CRC cell lines, as expected, we observed an increasing expression of NF–YAl from HT29 to RKO cells, hinting that NF–YAl expression could be involved in mesenchymal transition and aggressive phenotype (Suppl. Fig. 2).

These results together with the higher expression of NF–YAl in the CMS4 group prompted us to study possible effects on the EMT and ECM pathways induced by the overexpression of NF–YAs or NF–YAl in CRC HCT116 and HT29 cell lines (Fig. 2B and Suppl. Fig. 3A).

First, we investigated the consequences of NF-YA overexpression on the proliferative and clonogenic abilities of HCT116 and HT29 stable cell lines. While NF–YAs overexpression (NF-YAs^{high}) did not affect cell proliferation, NF–YAl-overexpressing cells (NF-YAl^{high}) showed a significant decrease in cell doubling, as highlighted by cell viability assay (Fig. 2C). Despite not statistically significant, a similar difference in cell proliferation between NF-YAs^{high} and NF-YAl^{high} was observed in HT29 cells (Suppl. Fig. 3B). Additionally, NF–YAl induced a striking reduction of anchorage-independent colony formation in both cell lines (Fig. 2D and Suppl. Fig. 3C). Further, we analyzed the behavior of 3D colonies grown from single cells seeded into Vitrogel that closely mimics the natural ECM. After 9 days of culture, NF-YAs^{high} HCT116 formed compact round colonies with increased dimension compared to empty cells. In opposition, NF-YAl^{high} HCT116 were not able to form polarized structures and showed larger irregular colonies (Fig. 2E).

According to the hypothesis of the existence of a balance between migration and proliferation in cancer cells [40], we investigated the migration abilities of HCT116 overexpressing cells. Transwell assays showed that high expression of both NF–YAl and NF–YAs enhances cell migration, with 3-fold increased migration of NF-YAl^{high} cells *versus* control cells (Fig. 2F). We observed the same behavior when we cultured the cells in Alvetex supports, highly porous polystyrene scaffolds designed for 3D cell culture. Both NF-YA isoforms, in particular NF–YAl, enhanced the depth of cell penetration into the scaffold (Fig. 2G).

3.3. NF–YAl overexpression triggers single-cell migration and single-cell detachment events

Wound healing assays and live imaging analysis further

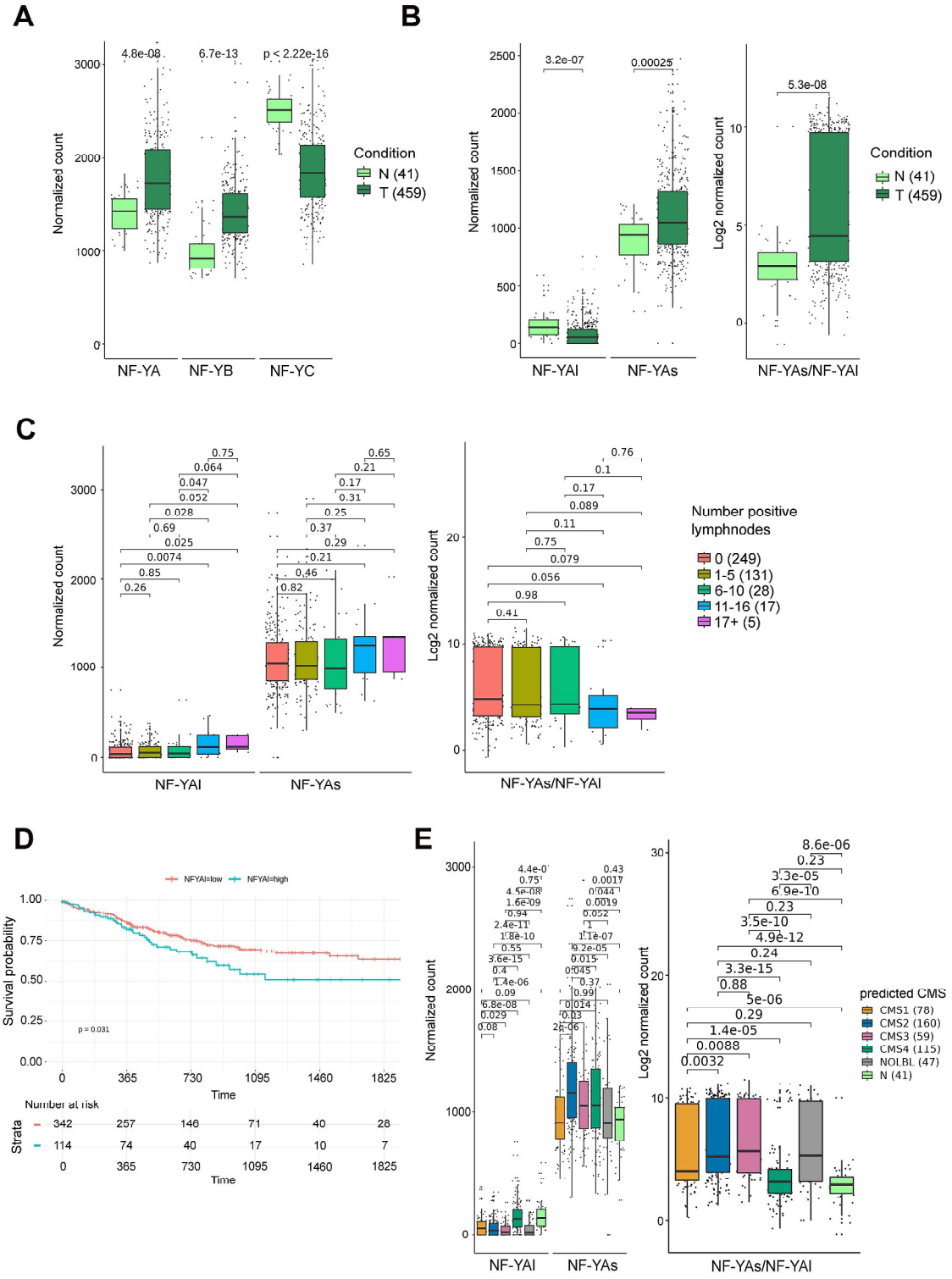

Fig. 1. Expression of NF-YA and its splice variants in CRC samples. A) Transcriptional levels of NF-YA, NF-YB and NF-YC subunits in tumor (T) tissue samples compared to normal (N) ones from the TCGA-COAD data set. Data are expressed as normalized count. P values were calculated with the Wilcoxon test. The number of patients for each condition is reported in brackets. B) Transcript levels of NF–YAl and NF–YAs isoforms (left) and ratio of NF–YAs/NF–YAl transcripts (right) in tumor (T) compared to normal (N) tissue samples from the TCGA-COAD data set. p values were calculated with the Wilcoxon test. The number of patients for each condition is indicated in brackets. C) Transcript levels of NF–YAl and NF–YAs (left) and NF–YAs/NF–YAl ratio (right) in COAD samples, stratified according to the number of positive lymph nodes. p values were calculated with the Wilcoxon test. The number of patients for each condition is reported in brackets. D) Kaplan–Meier analysis of survival progression measured as progression-free interval (PFI) in TCGA-COAD patients stratified according to high and low expression of NF–YAl. *P* value for the log rank test is indicated. E) Transcript levels of NF–YAl and NF–YAs isoforms (left) and of the NF–YAs/NF–YAl ratio (right) in COAD samples stratified according to Consensus Molecular Subtypes (CMS). NOLBL = samples without a defined CMS subtype. N = normal samples. P values were calculated with Wilcoxon test. The number of patients for each condition is reported in brackets.

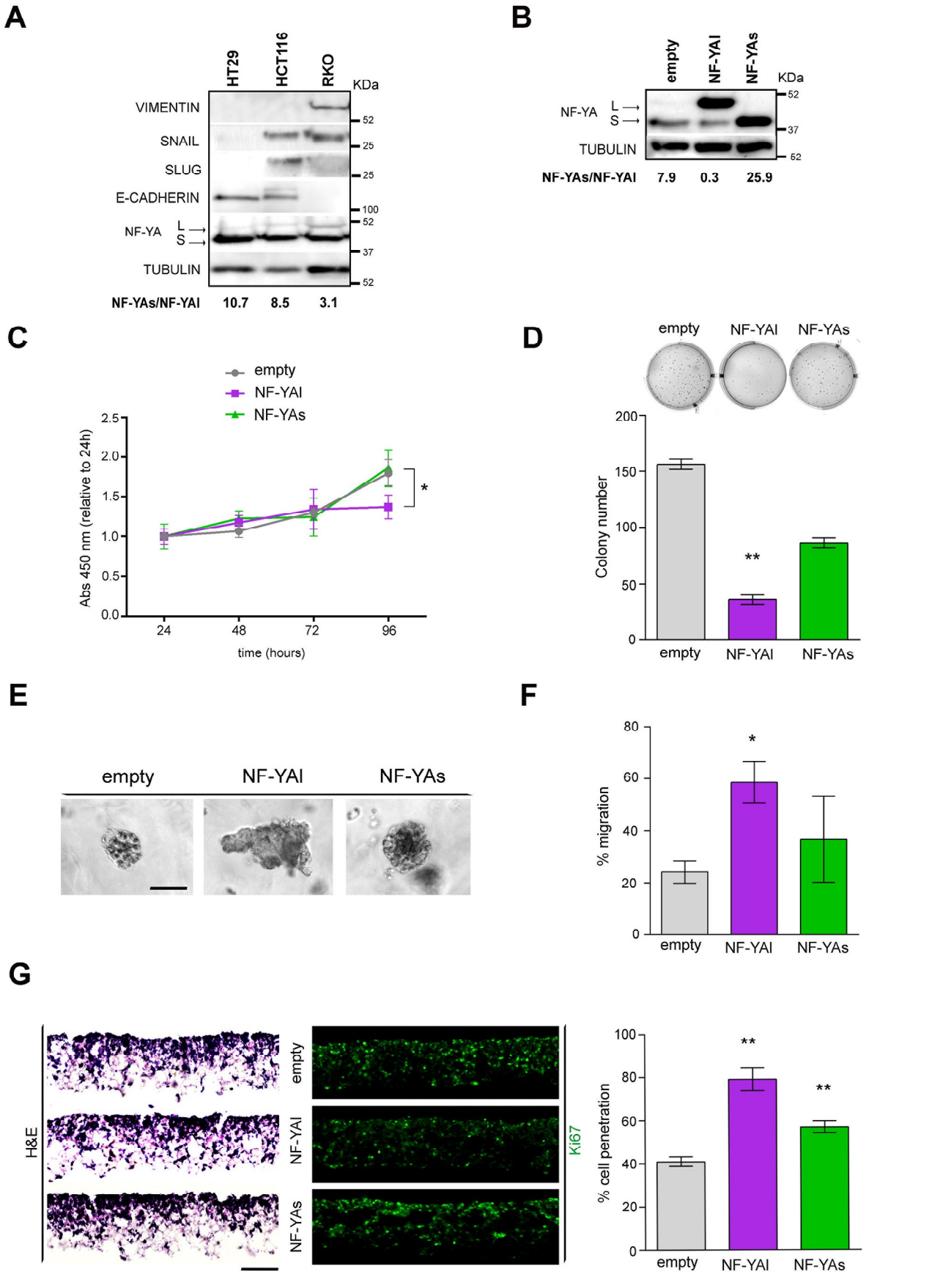

(caption on next page)

Fig. 2. Effect of NF-YA isoforms overexpression on proliferation and migration abilities of CRC cells. A) Western blot analysis of EMT markers (vimentin, snail, slug, E-cadherin) and NF-YA isoforms in CRC cell lines (HT29, HCT116, RKO). Tubulin was used as loading control. The quantification of NF–YAs and NF–YAl expression by ImageJ analysis is reported as NF–YAs/NF–YAl ratio. S = NF-YAs, L = NF–YAl. B) Protein levels of NF-YA isoforms measured by Western blot in HCT116 cells stably transduced with empty, NF–YAl and NF–YAs lentiviral particles. Tubulin was used as loading control. The quantification of NF-YAs and NF-YAl expression by ImageJ analysis is reported as NF–YAs/NF–YAl ratio. S = NF-YAs, L = NF–YAl. C) Cell proliferation curve of stably overexpressing HCT116 cells analyzed by PrestoBlue cell viability assay after 24, 48, 72, 96 h of growth. Data were normalized to 24 h time point and represent mean ± SEM (one-way ANOVA: *p < 0.05 vs empty, n = 3). D) Colony number of Empty, NF–YAl and NF–YAs stable HCT116 cells in anchorage-independent condition. Data represent mean ± SEM (one-way ANOVA: **p < 0.01 vs empty, n = 3). E) Optical microscopy images representing Empty, NF–YAs and NF–YAl 3D colonies morphology in Vitrogel matrix. Scale bar: 200 μm. F) Percentage of cell migration of Empty, NF-YAl^{high} and NF-YAs^{high} cells measured by transwell assay. Data represent mean ± SEM (one-way ANOVA: *$p < 0.05$, $n = 3$). G) Left: representative images of Alvetex cryosections stained with H&E and immunostained with Ki67 (green); scale bar: 100 μm. Right: percentage of cell penetration of Empty, NF-YAl^{high} and NF-YAs^{high} cells in Alvetex scaffold after 72 h. Data represent mean ± SEM (one-way ANOVA: **p < 0.01 vs empty. n = 3).

demonstrated higher migration abilities of both HCT116 and HT29 NF-YAl^{high} cells (Fig. 3A; Movies 1-3, Suppl. Fig. 3D). Particle image velocimetry (PIV) analysis on cell migration in HCT116 showed increased speed of flows within cell sheet of NF-YAl^{high} cells compared to NF-YAs^{high} ones (Fig. 3B). Interestingly, while the leading edge advanced steadily forward in NF-YAs^{high} HCT116 cells, NF-YAl^{high} cells showed a disordered progression, as highlighted also by the complexity parameter L/D (Fig. 3C). This difference was corroborated by measurements of directionality within the cells sheet. As shown by angular deviation and variance, NF–YAs overexpression induced the cells to flow into the space at the sheet edge, differently from NF-YAl^{high} cells that migrated in multiple directions and with an angular direction farther from the perpendicular to the front edge (Fig. 3D).

Supplementary video related to this article can be found at https://doi.org/10.1016/j.canlet.2023.216262

These results suggested that collective migration occurs in NF-YAs^{high} cells, while more disordered motion at the leading edge, reminiscent of single cell migration, characterizes NF-YAl^{high} cells. Cancer cells disseminate as individual cells *via* mesenchymal or amoeboid modes, with the amoeboid state being considered a mechanism to acquire further plasticity and overcome certain environmental challenges, such as confined migration through narrow spaces and smaller pores of the ECM. High resolution microscopy images clearly showed the presence of cells with amoeboid-like morphology at the migrating edge of NF-YAl^{high} cells, but not of control or NF-YAs^{high} ones (Fig. 3E). Consistently, live cell analysis of wound healing highlighted the presence of NF-YAl^{high} cells migrating through amoeboid-like movement (Movie 4). We observed the same migration style in NF-YAl^{high} cells, but not in NF-YAs^{high}, when cultured in non-confluent 2D conditions (Movies 5,6).

Supplementary video related to this article can be found at https://doi.org/10.1016/j.canlet.2023.216262

To determine whether the different modalities of migration have implications for cell dissemination from primary tumors, we transferred pre-formed spheroids on collagen substrate (Fig. 3F). Empty and NF-YAs^{high} cells showed cells "wetting" the substrate out but in close proximity of the spheroid body. In opposition, single cells disseminated from NF-YAl^{high} spheroids into the substrate. To better explore this phenomenon, 3D spheroids formed in Matrigel matrix were transferred into flat-bottom multi-well tissue culture plates, and time-lapse microscopy was used to detect cells detaching from the spheroid surface into free space (Fig. 3G.). Compared to the spheroids composed of empty HCT116, more cells migrated collectively from the NF-YAs^{high} spheroid with few single cells visible at the front of migrating cells, while NF-YAl^{high} cells moved individually and left the spheroid body (Movies 7,8,9, Fig. 3G).

Supplementary video related to this article can be found at https://doi.org/10.1016/j.canlet.2023.216262

3.4. NF-YAl^{high} cells have infiltration ability in vitro and high metastatic dissemination in vivo

To further demonstrate that increased NF–YAl expression favors cell invasion abilities, we compared the extent of infiltration of NF-YAl^{high}, NF-YAs^{high} and empty cells into a monolayer of primary human fibroblasts (HFF). Stably transduced HCT116 and HFF were cultured in adjacent compartments of a silicone insert that was removed when the cells reached confluence, enabling both cancer cells and fibroblasts to migrate towards each other (Fig. 4A). After 72 h from insert removal, NF-YAl^{high} cancer cells infiltrated into the stromal monolayer. Interestingly, also HFF cells scattered into NF-YAl^{high} HCT116 population, suggesting that high NF–YAl expression could attract stromal cells.

We then studied the dissemination properties of CRC cell lines using the Tg(fli1:EGFP) zebrafish *in vivo* model. Empty, NF-YAs^{high} and NF-YAl^{high} HCT116 cells were injected separately in the perivitelline space to simulate the tumor mass. As previously demonstrated *in vitro*, NF-YAl^{high} cells showed higher migration properties in comparison to NF-YAs^{high} cells (Fig. 4B). Empty and NF-YAs^{high} cells showed similar percentages of embryos with circulating cells, 56.19% and 51.02%, respectively, while NF-YAl^{high} cells reached the 72.67%. Next, we decided to co-inject NF-YAs^{high} and NF-YAl^{high} cells, in order to better simulate cell sub-clones heterogeneity (Fig. 4C). Also in these experimental conditions, NF-YAl^{high} cells exhibited higher migration capability: 37.26% of the embryos ($p = 0.04$) had uniquely NF-YAl^{high} metastasizing cells, while 17.78% of the embryos had both NF-YAs^{high} and NF-YAl^{high} cells dissemination. Surprisingly, we did not identify embryos with only NF-YAs^{high} cells.

3.5. NF-YAl^{high} and NF-YAs^{high} cells show a different ECM-related and EMT-related gene signature

A combination of strong cell-matrix and weak cell-cell adhesions could account for increased invasion abilities of NF-YAl^{high} cells. In opposition to collective motility that requires coordinated cell–cell interactions, individual cell migration relies on weakened intercellular adhesion, and changes in ECM properties could promote EMT and mesenchymal-to-amoeboid transition [42]. To explore this hypothesis, we performed RT-qPCR analysis using a predesigned 96-well panel to profile the expression of ECM and adhesion molecules in NF-YAs^{high} and NF-YAl^{high} HCT116 compared to empty cells. While only few genes were modulated by NF–YAs, NF–YAl forced expression triggered the transcriptional up-regulation of multiple genes belonging to peptidase, collagen, integrin, laminin and ECM families (Fig. 5A and Suppl. Fig. 4). Interestingly, the majority of the genes up-regulated in NF-YAl^{high} cells have significant higher transcription levels in the CMS4 CRC subtype in comparison with the other classes (Fig. 5B). Additionally, we observed an increase in mRNA levels of key EMT genes, such as Snai1, Fibronectin1 and Tgfβ in NF-YAl^{high} cells (Fig. 5C).

To determine whether NF–YAl could directly control the expression of the above-described ECM-related and EMT genes, we first examined their regulatory regions for the presence of NF–Y binding sites (Fig. 5D). Despite the enrichment in the NF–Y motif in both ECM and EMT genes, most of the ECM genes up-regulated in NF-YAl^{high} cells did not show direct NF–Y binding from ENCODE data at UCSC, which tracks transcription factor binding to DNA elements by ChIP-seq. Since these data do not include CRC cells, we performed qChIP (quantitative Chromatin ImmunoPrecipitation) in HCT116 cells. We confirmed that NF–Y does not bind to the CCAAT-binding motif in the promoter of fibronectin 1

gene. Differently, we validated the binding of NF–Y on the EMT genes Snai1 and Snai2 (Fig. 5E). Beyond the up-regulation of the canonical EMT-TFs SNAIL and SLUG (Fig. 5F), we identified an increase in the expression of the Rho family of GTPases, RhoA and RhoC, which regulate cell motility through effects on actin and microtubule dynamics, myosin activity and cell-ECM/cell–cell adhesions [43], in both NF-YAl^{high} and NF-YAs^{high} cells (Fig. 5F). Differently, we observed a major effect induced only by NF–YAl on the phosphorylation of Akt, known to have a role in EMT and cell migration [44]. Total extracts from spheroids showed the same expression pattern, except for RhoC (Fig. 5F, right panel).

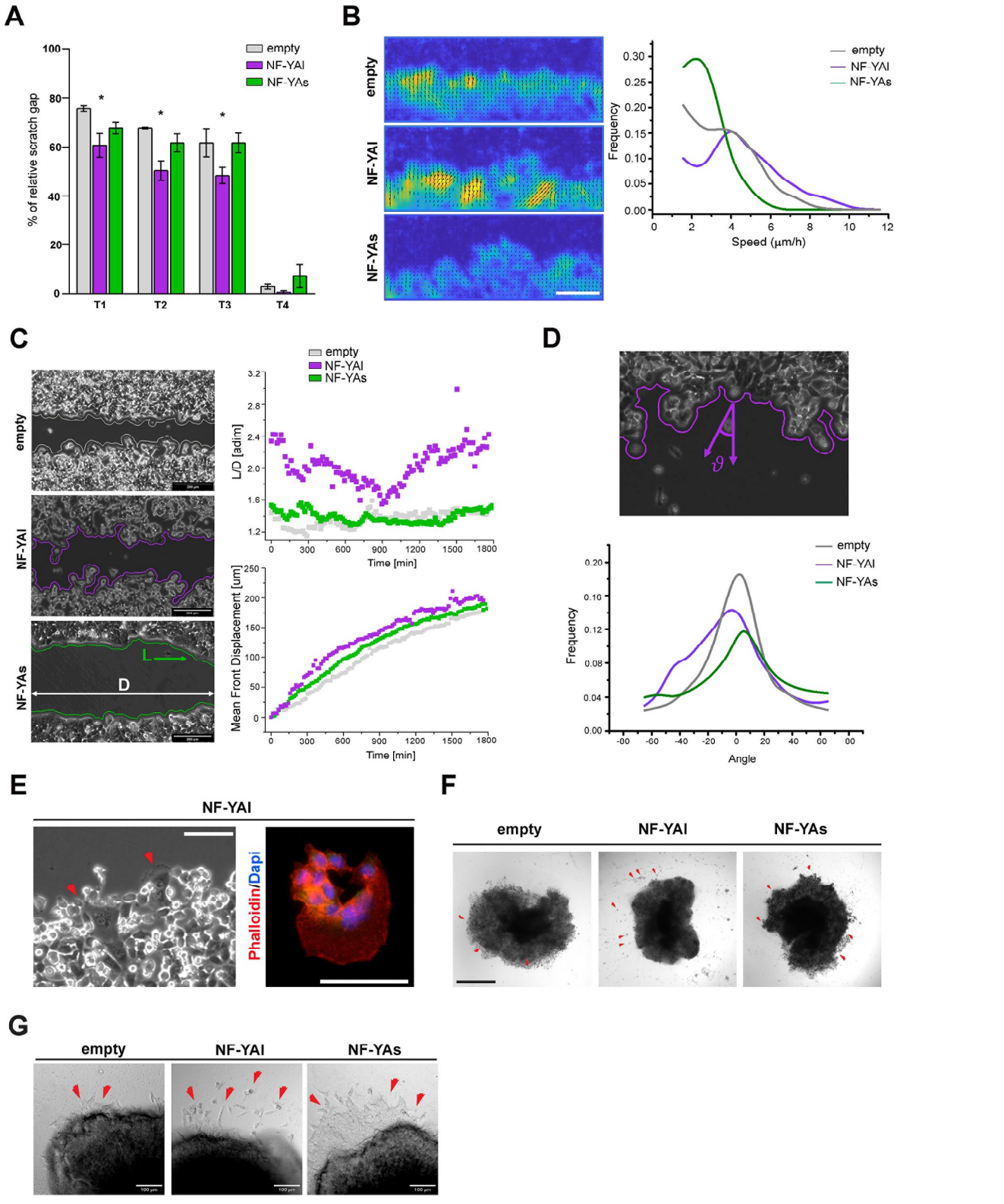

(caption on next page)

Fig. 3. Effects of stable overexpression of NF-YA isoforms on cell migration mode and dissemination. A) Ibidi wound healing assay on empty, NF–YAl and NF–YAs overexpressing HCT116 cells: quantification of the wound area compared to the initial gap, arbitrarily set at 100%, after 16 h (T1), 24 h (T2), 30 h (T3), 48 h (T4). Data represent mean ± SEM (one-way ANOVA: *$p < 0.05$, $n = 3$). B) Left: PIV (Particle Image Velocimetry) plots of the advancing edge of empty, NF–YAl and NF–YAs cells in a wound healing experiment. The false-color scale represents the comparison of the cell motion speed (the lighter regions are areas with faster migration speed whereas the vectors also represent the velocity direction. Scale bar: 200 μm. Right: the speed distribution plot for the three different cell populations is reported. C) Left: snapshots of the wound healing experiments for empty, NF-YAl^{high} and NF-YAs^{high} cells. The images show the reconstructed advancement front. L is the effective front length whereas D is the width of the imaged area. Right: L/D ratio as a function of time is reported for the different cell populations together with the average displacement of the cell fronts. D) Analysis of migration direction of the different cell populations. Upper panel: the direction angle is defined with respect to the perpendicular to the average cell front. Lower panel: the distributions of the cell migration directions are reported for the different cells. E) Left: snapshot of movie 4 representing cell front in the wound healing assay of NF-YAl^{high} cells. Scale bar: 200 μm. Right: high resolution microscopic image of NF-YAl^{high} cells immunostained with phalloidin (red) and dapi (blue). Scale bar: 50 μm. F) Representative images of empty, NF–YAl- and NF–YAs-overexpressing MTSs formed in Matrigel matrix and then transferred on collagen substrate. Red arrows indicate cells migrating from spheroids. Scale bar: 300 μm. G) Snapshots of movie 7, 8, 9 representing cell detachment and dissemination (red arrows) from empty, NF-YAl^{high} and NF-YAs^{high} MTSs moved into flat bottom well plate. Scale bar: 100 μm.

3.6. NF–YAl and NF–YAs oppositely regulate E-cadherin gene expression

Although qChIP and RT-qPCR assays demonstrated a direct role for NF–Y in the regulation of some EMT genes, they did not account for the diversity in the modes of cell migration observed in NF-YAl^{high} and NF-YAs^{high} cells. Therefore, we focused our attention on the Cdh1 gene, encoding for E-cadherin, an adherens junction protein fundamental in coordinated and collective migration [45]. We observed a significant decrease in protein and mRNA levels of E-cadherin in NF-YAl^{high} cells (Fig. 6A and B). Oppositely, NF-YAs^{high} cells showed increased expression of E-cadherin when cultured as 3D spheroids (Fig. 6A, right panel). The analysis of E-cadherin staining by immunofluorescence confirmed lower levels together with partial cytoplasmic delocalization in NF-YAl^{high} cells (Suppl. Fig. 5). Similarly, E-cadherin levels were reduced in NF-YAl^{high} and increased in NF-YAs^{high} HT29 cells (Suppl. Fig. 3E). These results hinted that E-cadherin could be one of the NF–Y targets differently controlled by NF-YA isoforms. qChIP identified both NF-YA and NF-YB subunits on the promoter of the E-cadherin gene in HCT116 cells (Fig. 6C). The analysis of NF-YA binding in NF-YAl^{high} and NF-YAs^{high} cells clearly showed that both isoforms increase the recruitment of the NF–Y complex onto chromatin, regardless of which isoform is overexpressed (Fig. 6D), thus ruling out that gene repression observed in NF-YAl^{high} cells depends on the loss of NF–Y binding.

The luciferase reporter assay highlighted a significant decrease and increase of the Cdh1-promoter activity in NF-YAl^{high} and in NF-YAs^{high} cells, respectively, when compared to empty ones (Fig. 6E). The reduced activity could be the consequence of direct gene repression mediated by the NF–YAl-containing NF–Y complexes, rather than an indirect effect induced by other proteins modulated in NF-YAl^{high} cells. To explore these hypotheses, we co-transfected the Cdh1 promoter reporter vector with NF–YAs in NF-YAl^{high} cells and *vice versa*. The activity of the Cdh1 promoter in NF-YAl^{high} cells increased following NF–YAs overexpression, in opposition to the decrease induced by NF–YAl in NF-YAs^{high} cells (Fig. 6E). These results suggested that a competition occurs between NF–YAs and NF–YAl in the regulation of the Cdh1 target gene.

Transient transfection of a DNA-binding NF-YA mutant (NF-YA-DN), working as a dominant repressor of NF–Y-DNA complex formation, further clarified the activity of NF-YA isoforms on Cdh1 promoter regulation (Fig. 6F) [46]. The dose-response decrease in luciferase activity triggered by NF-YA-DN in control HCT116 cells, demonstrated that the endogenous NF–Y heterotrimer, primarily composed of the NF–YAs isoform, works as transcriptional activator on the E-cadherin gene. We observed a similar trend in NF-YAs^{high} cells, although to a lesser extent, presumably because higher NF–YAs expression reduces the effect of the dominant negative. Differently, the NF-YA-DN mutant did not affect the luciferase activity in NF-YAl^{high} cells. The analysis of chromatin extracts from transduced HCT116 provided a possible explanation to this result (Fig. 6G): since both endogenous NF–YAs and overexpressed NF–YAl are recruited onto chromatin, the competition of the NF-YA-DN with both isoforms could affect both NF–YAs-induced activation and NF–YAl-mediated repression, hence resulting in no transcriptional effects on Cdh1 gene transcription.

In addition to the transcriptional regulation, the expression of E-cadherin is controlled by protein stability [47,48]. The analysis of E-cadherin by Western blot and RT-qPCR highlighted decoupled mRNA and protein levels, suggesting an additional non-transcriptional mechanism in NF-YAl^{high} cells. Indeed, cell treatments with proteasome and lysosome inhibitors (MG132 and Chloroquine, respectively) partially rescued the robust protein decrease previously observed in NF-YAl^{high} cells and further increased E-cadherin protein levels in NF-YAs^{high} cells (Fig. 6H).

Taken together, these results demonstrate that the two NF-YA isoforms can oppositely control gene expression by direct chromatin recruitment on target genes. Among NF–Y target genes, E-cadherin repression mediated by NF–YAl can be responsible of the aggressive phenotype observed in NF-YAl^{high} cells.

4. Discussion

The EMT process has an undisputed role in promoting invasiveness, metastatic ability and drug resistance in cancer cells [49]. EMT accompanies the dissemination of epithelial cells through the disruption of adherens and tight junctions. Moreover, the expression of mesenchymal markers promotes interaction with the ECM to enhance cell migration and intravasation. Surviving circulating tumor cells eventually extravasate into distant organs and give rise to metastases [50]. In the last years, many studies showed the occurrence of partial/intermediate/hybrid EMT phenotypes that may be even more effective than a complete EMT in metastatic cell dissemination [51,52].

The expression of the NF-YA subunit and its splice variants has already been shown to be altered in various tumor types. In particular, Mantovani's group showed the existence of a NF-YAl^{high}-Claudin^{low} signature associated with low levels of basal keratins and high EMT markers in basal-like aggressive breast tumors [13].

Here we showed that NF–YAl commonly decreases in CRC tissues in opposition to NF–YAs, except for the CMS4 mesenchymal subtype that shows normal NF–YAl levels and lower NF–YAs/NF–YAl ratio compared to other CMSs.

HCT116 CRC cells, which have higher levels of NF–YAs compared to NF–YAl, represent a good model to investigate the effect of increased NF–YAl expression. The comparison between engineered HCT116 overexpressing NF–YAs or NF–YAl highlighted different cell proliferation and migration behaviors. NF-YAs^{high} cells form compact and well-organized spheroids that are bigger than control cells when cultured in VitroGel Hydrogel Matrix, which closely mimics the natural ECM environment. In opposition, NF-YAl^{high} cells show reduced 2D cell proliferation and form irregular-shaped spheroids when cultured in 3D, hinting at loss of homotypic cell adhesion. For epithelial cells, multicellular spheroid formation is primarily mediated by E-cadherin-containing adherens junctions [53]. In agreement with this, we detected different levels of E-cadherin expression in NF- YAl^{high} and NF- YAs^{high} cells cultured in both 2D and 3D conditions.

The different expression of E-cadherin is also consistent with the diverse mode of migration observed in engineered HCT116 cell lines.

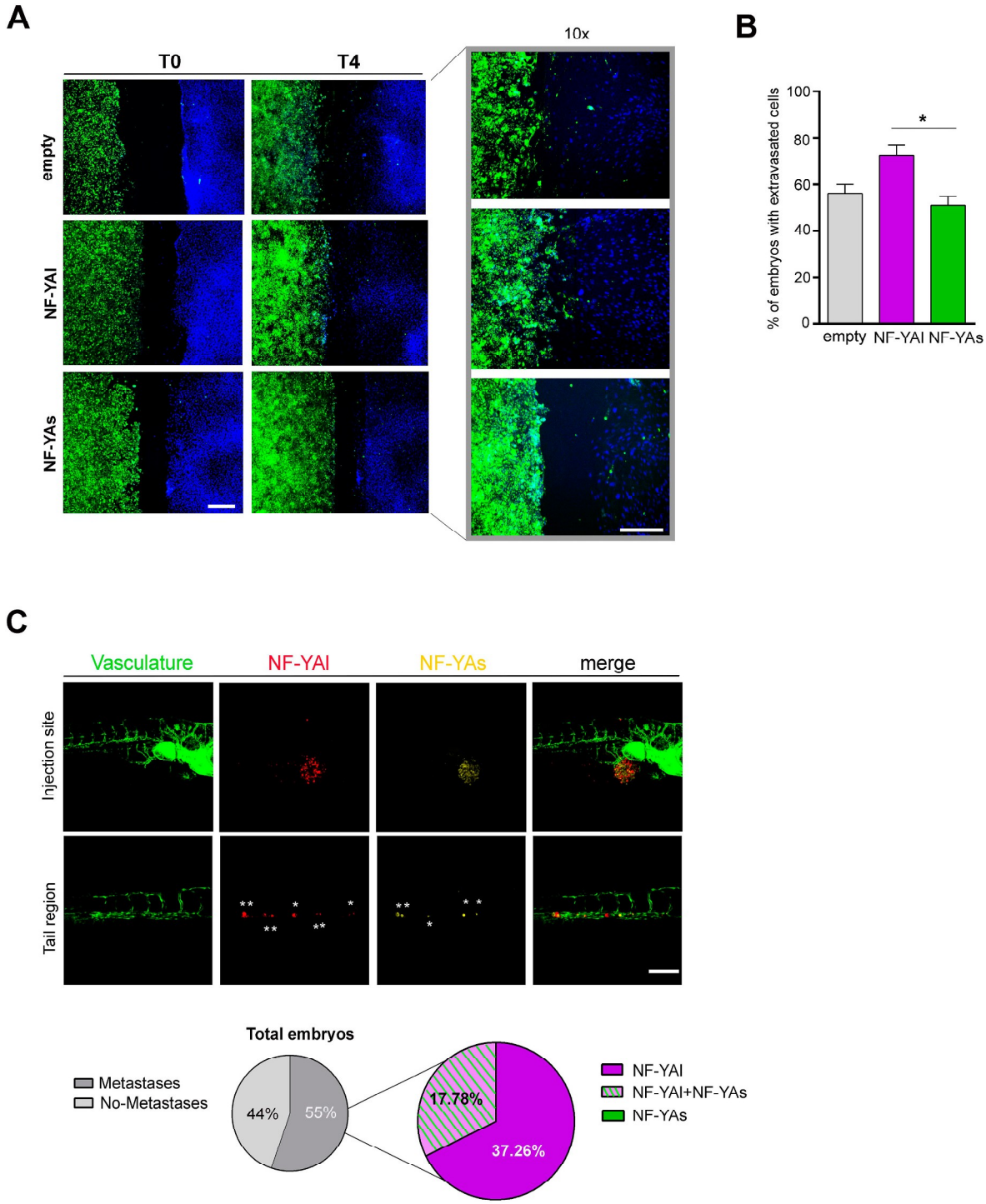

Fig. 4. NF-YA isoforms overexpression effect on infiltration ability *in vitro* and metastatic dissemination *in vivo*. A) Ibidi wound healing assay on empty, NF-YAl^{high} and NF-YAs^{high} HCT116 cells stained with Vibrant DiO Cell-Labeling (green) and HFF stained with dapi (blue). Cell infiltration was observed up to 72 h (T4) after insert removal (T0). Scale bar: 500 μm (T0, T4). 10x: 200 μm. B) Percentage of Tg(fli1: EGFP) zebrafish embryos with extravasated cells after injection of empty, NF-YAl^{high} or NF-YAs^{high} HCT116 cells. Data represent mean ± SEM (multiple Student t-test: *p < 0.05). C) Upper panel: immunofluorescence images of cell dissemination of NF-YAl^{high} (red) and NF-YAs^{high} (yellow) HCT116 cells after co-injection in zebrafish embryos (green). Scale bar: 500 μm. Lower panel: percentage of embryos with metastasis and percentage of metastasis formed by NF–YAl, NF–YAs, or both NF–YAl/NF–YAs cells.

High NF–YAl levels support cell dissemination by adopting heterogeneous mesenchymal and amoeboid single cell strategies, while collective migration distinguishes NF-YAs^{high} cells. Collective migration is characterized by groups of cells that retain cell-cell adhesion and E-cadherin expression, and commonly leads to local invasion of cancer cells. In opposition, the formation of distant metastatic lesions requires the loss of intercellular interactions that enable individual cancer cells or small cell clusters to detach from the primary tumor, penetrate blood or lymphatic vessels and extravasate in distant organs [54,55]. This behavior is consistent with the higher number of zebrafish metastatic embryos following the injection of NF-YAl^{high} *versus* NF-YAs^{high} cells in the perivitelline space. The increased metastatic ability of NF-YAl^{high} is

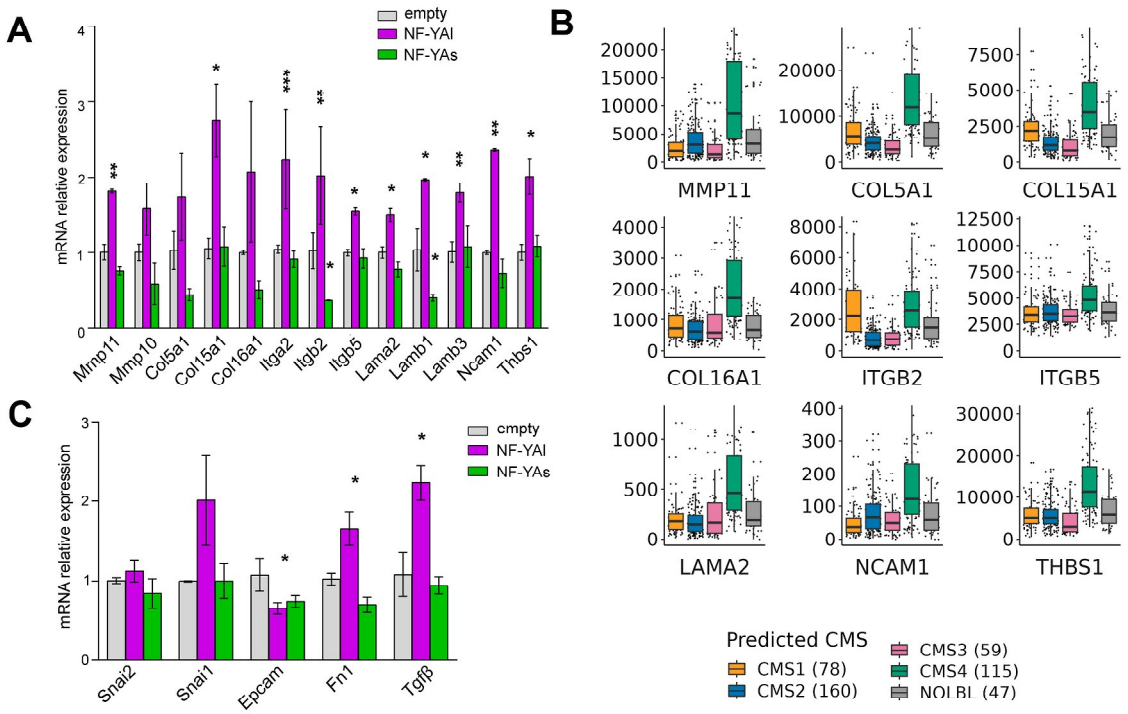

D

	GENE	CCAAT sequence	NF-Y motif	NF-Y binding in ENCODE ChIPseq
ECM	*MMP11*	no	no	no
	MMP10	yes	yes	no
	COL5A1	yes	yes	yes
	COL15A1	yes	yes	no
	COL16A1	yes	yes	no
	ITGA2	no	yes	no
	ITGB2	yes	yes	no
	ITGB5	yes	yes	no
	LAMA2	no	yes	no
	LAMB1	no	no	no
	LAMB3	yes	yes	no
	FN1	yes	yes	no
	NCAM1	no	no	no
	THBS1	yes	yes	yes
EMT	*CDH1*	yes	yes	yes
	SNAI1	yes	yes	yes
	SNAI2	yes	yes	yes
	EPCAM	no	no	no
	TGFB1	yes	yes	no

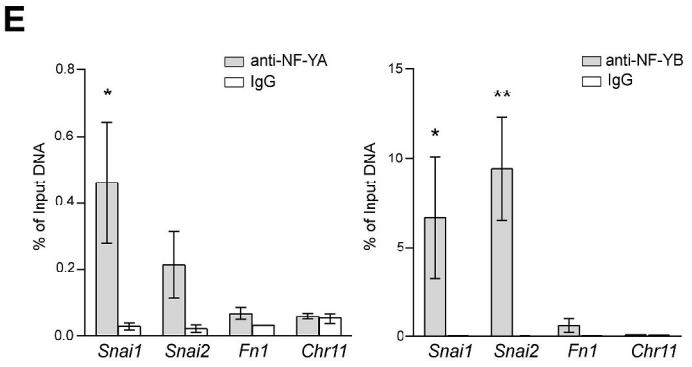

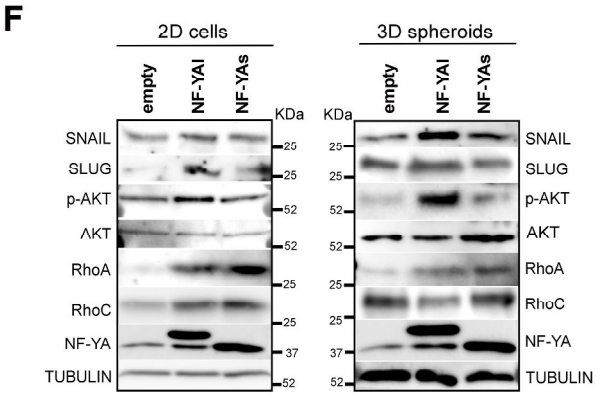

Fig. 5. Transcriptional regulation of EMT and ECM genes in HCT116 overexpressing cells. A) RT-qPCR analysis of genes selected from Extracellular Matrix & Adhesion Molecules predisigned 96-well plate Bio-Rad (Suppl. Fig. 4) in NF-YAs^{high} and NF-YAl^{high} HCT116 compared to empty cells. Data represent mean ± SEM (one-way ANOVA: *p < 0.05, n = 2). B) Transcript levels (normalized counts) of selected genes related to ECM and adhesion molecules in COAD samples stratified according to the Consensus Molecular Subtypes (CMS). C) mRNA levels of EMT genes measured by RT-qPCR in NF-YAs^{high} and NF-YAl^{high} HCT116 compared to empty cells. Data represent mean ± SEM (one-way ANOVA: *p < 0.05, n = 4). D) In silico analysis of selected promoters (−950bp to +50bp relative to TSS) for the presence of the CCAAT pentanucleotide or putative NF–Y transcription factor binding sites (Jaspar and Transfac matrices). The right column indicates the possible NF–Y binding from ENCODE ChIP-seq datasets at UCSC (http://genome.ucsc.edu/ENCODE/). E) qChIP analysis of NF-YA (left) and NF-YB (right) binding to promoter regions of *Snai1, Snai2, Fn1* genes in HCT116 cells. The satellite heterochromatin region of chromosome 11 (Chr 11) has been used as negative control region and IgG as a negative control antibody. Data represent mean ± SEM (ANOVA with Fisher's LSD test: *p < 0.05, **p < 0.01, n = 5). F) Western blot analysis of Snail, Slug, *p*-AKT and total AKT, RhoA, and RhoC in 2D (left) and 3D (right) empty, NF-YAl^{high} and NF-YAs^{high} cells. Tubulin was used as loading control.

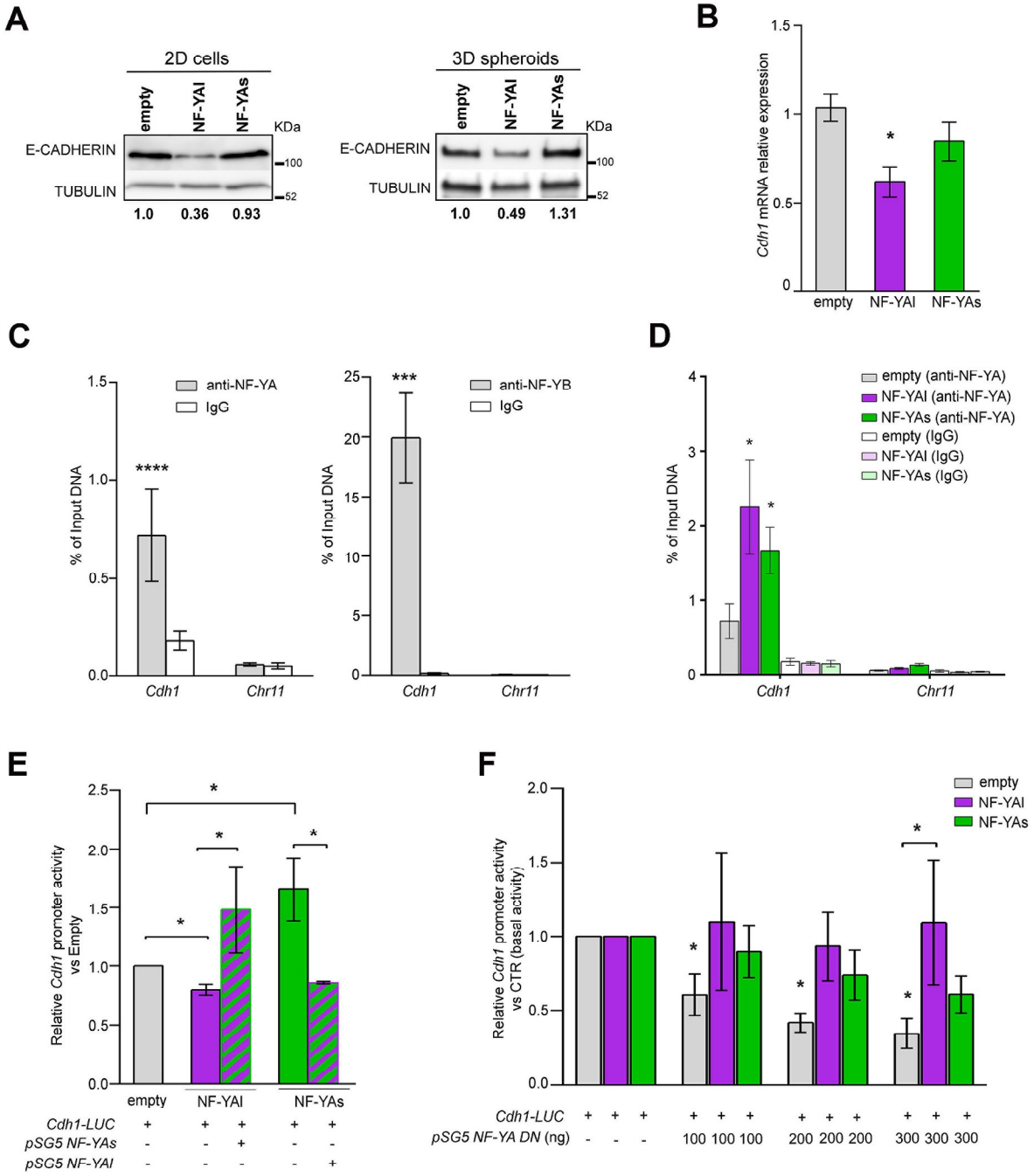

(caption on next page)

Fig. 6. Regulation of the E-cadherin gene by NF-YA splicing isoforms. A) Western blot analysis of E-cadherin protein levels in 2D (left) and 3D (right) empty, NF-YAl^{high} and NF-YAs^{high} cells. Tubulin was used as loading control. The quantification of E-cadherin levels by Image J analysis is reported as normalized to Tubulin and relative to empty, arbitrarily set at 1. B) mRNA levels of *Cdh1* gene measured by RT-qPCR in NF-YAs^{high} and NF-YAl^{high} HCT116 compared to empty cells. Data represent mean ± SEM (one-way ANOVA: *p < 0.05, n = 4). C) qChIP analysis of NF-YA (left) and NF-YB (right) binding to promoter region of *Cdh1* gene in HCT116 cells. The satellite heterochromatin region of chromosome 1 (Chr 11) has been used as negative control region and IgG as a negative control antibody. Data represent mean ± SEM (Student t-test: ***p < 0.001, ****p < 0.0001, n = 5). D) qChIP analysis of NF-YA binding to promoter region of *Cdh1* gene in empty, NF-YAl^{high} and NF-YAs^{high} cells. Data represent mean ± SEM (Student t-test: *p < 0.05, n = 5). E) *Cdh1* gene promoter activity measured by luciferase reporter assay in empty, NF-YAl^{high} and NF-YAs^{high} HCT116 cells following the co-tranfection of pSG5-NF-YAs or pSG5-NF-YAl. Data represent mean ± SEM (one-way ANOVA with Fisher's LSD test: *p < 0.05, n = 4). F) *Cdh1* gene promoter activity after transient co-transfection of empty, NF-YAl^{high} and NF-YAs^{high} cells with Cdh1-LUC vector and the DNA-binding NF-YA mutant (NF-YA-DN) at different concentrations (100, 200, 300 ng). Data represent mean ± SEM (Two-way ANOVA with Fisher's LSD test: *p < 0.05, n = 7). G) Protein levels of NF-YA isoforms measured by Western blot in soluble nuclear and chromatin-enriched cell extracts of empty, NF-YAl^{high} and NF-YAs^{high} HCT116 cells. Actin and histone H3 were used as loading controls. H) Western blot analysis of E-cadherin protein levels in empty, NF-YAl^{high} and NF-YAs^{high} cells treated for 16 h with the proteasome (MG132, 50 μM) and lysosome (Chloroquine, 10 μM) inhibitors. Tubulin was used as loading control. The quantification of E-cadherin levels by Image J analysis is reported as normalized to Tubulin and relative to empty, arbitrarily set at 1.

further corroborated by the co-injection of NF-YAl^{high} and NF-YAs^{high} cells, which can mimic the clonal heterogeneity within a tumor mass. While we detected metastatic embryos with only NF-YAl^{high} cells (about 40%) or both NF-YAl^{high} and NF-YAs^{high} cells (about 20%), there were no embryos containing NF-YAs^{high} cells uniquely. This phenomenon could be the consequence of the different behavior of the two cell types in the neoplastic ecosystem that we already observed in prostate cancer [14]: NF-YAs^{high} cells are highly proliferating and allow tumor growth, whereas NF-YAl^{high} cells represent circulating tumor cells, pre-metastatic populations that give rise to distant metastases.

In breast cancer, of the 11 upregulated EMT genes analyzed in NF-YAl^{high}-Claudin^{low} cells, Mantovani's group identified the CCAAT box and NF–Y binding only in the TGFBR2 promoter, a bona fide target gene [56]. Hence, they concluded that NF-YAl^{high} participates in EMT through indirect mechanisms. Differently, our chromatin immunoprecipitation analysis shows that NF–Y can directly control the transcription of some key EMT genes and can induce a hybrid EMT state in CRC cells. In particular, NF–YAl seems to be more active in Snai2 transactivation and Cdh1 repression. NF–Y ability to function as both transcriptional activator and repressor has already been shown and it relies on the recruitment onto chromatin of co-activators or co-repressors [35,36,57,58]. Considering that exon 3 splicing has no effect on the DNA binding domain of NF-YA isoforms, it was not surprising to detect similar binding of NF-YA to the Cdh1 promoter in NF-YAl^{high} and NF-YAs^{high} cells. Further studies will allow to better characterize the repressive complex recruited together with NF–YAl on the regulatory regions of the Cdh1 gene.

Consistent with multiple interactions occurring between EMT, epithelial polarization, cell migration and ECM, NF-YAl^{high} cells are characterized by significant modulation of the transcriptional profile of extracellular matrix and adhesion molecules genes. Of the 19 genes differentially expressed upon NF–YAl overexpression, 15 contain NF–Y binding motives in their promoter regions, which implies a possible direct role for NF–Y in ECM regulation.

Finally, we should not forget that mechanisms other than direct regulation by transcription factors participate in EMT regulation. Epigenetic modifications, alternative splicing, microRNA-mediated gene silencing, translation initiation and protein degradation mechanisms play a critical role in this process [59–61], suggesting that NF–Y and its splice variants could participate in EMT in multiple ways. Consistently with this hypothesis, it is well documented that NF–Y is a pioneer transcription factor that drives epigenetic mechanisms and also controls the expression of proteasome subunits and activity [62,63]. In agreement with this, the robust decrease in E-cadherin protein levels observed in NF-YAl^{high} cells is partially rescued by the administration of proteasome and lysosome inhibitors.

Although loss and gain of function experiments in cell lines are effective strategies to identify proteins activity, we are aware that they do not exactly mimic the conditions observed in patients. However, the integration of the results obtained from overexpressing cells and large-scale biological datasets clearly suggests that the distinct levels of NF-YA isoforms in CRC subtypes are associated with diverse cellular and molecular phenotypes, which may be at least in part established through the specific activity of NF–YAl or NF–YAs.

Altogether, our study shows that high NF–YAl transcription levels can stratify CRC patients and predict their poor overall survival, similarly to CMS subtyping. Tumor cells with high NF–YAl expression acquire enhanced single-cell migratory and invasive potential, most likely as the consequence of low E-cadherin expression (Fig. 7). NF–YAl to NF–YAs splice-switching strategies based on antisense oligonucleotides (ASOs) could be a powerful approach to alter the NF–YAs/NF–YAl ratio and, consequently, inhibit the metastatic potential of CRC cells.

Consent for publication

Not applicable.

Ethics approval

Tg(fli1:EGFP) transgenic zebrafish strain was handled in compliance with local animal welfare regulations (authorization n. prot. 18311/2016; authorization for zebrafish breeding in IRST facility released by the "Comune di Meldola", November 09, 2016) and in conformity with the Directive 2010/63/EU.

Availability of data and materials

The corresponding author will provide data and reagents used in this study upon request.

Disclaimer

Funded by the European Union. Views and opinions expressed are however those of the authors only and do not necessarily reflect those of the European Community or European Union. Neither the European Union nor the European Community can be held responsible for them.

CRediT authorship contribution statement

Giovanna Rigillo: Conceptualization, Data curation, Formal analysis, Investigation, Methodology, Writing - original draft. **Silvia Belluti:** Conceptualization, Data curation, Formal analysis, Investigation, Methodology, Writing – review & editing. **Virginia Campani:** Formal analysis, Investigation, Methodology, Validation. **Gregorio Ragazzini:** Methodology. **Mirko Ronzio:** Data curation, Formal analysis. **Giacomo Miserocchi:** Investigation, Methodology. **Beatrice Bighi:** Methodology. **Laura Cuoghi:** Methodology. **Valentina Mularoni:** Methodology. **Vincenzo Zappavigna:** Writing – review & editing. **Diletta Dolfini:** Formal analysis, Supervision. **Laura Mercatali:** Supervision. **Andrea Alessandrini:** Conceptualization, Investigation, Supervision, Writing – original draft. **Carol Imbriano:** Conceptualization, Funding acquisition, Project administration, Supervision, Writing – original draft.

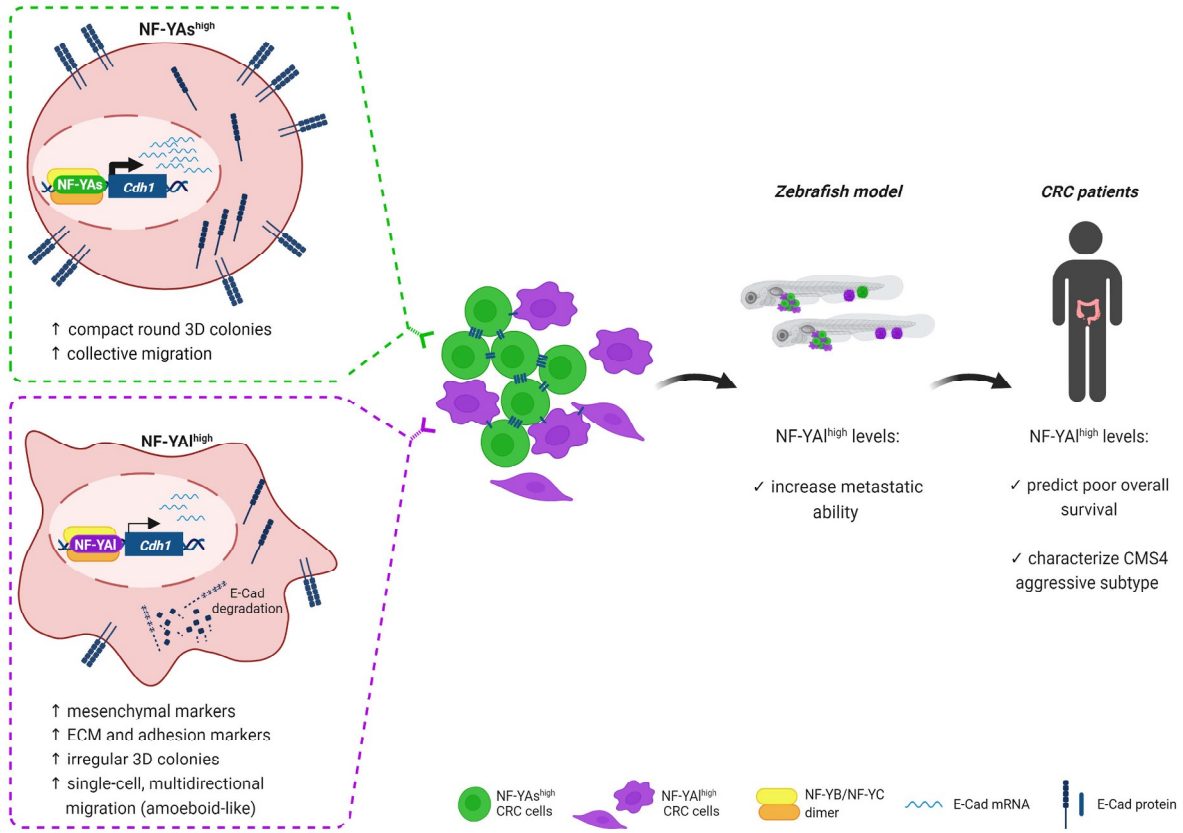

Fig. 7. Overview of the molecular activity and clinical implications of high NF–YAl or NF–YAs expression in CRC. High expression of NF–YAs and NF–YAl differently modulates the transcription of ECM- and EMT-related genes. In particular, direct transcriptional regulation of E-Cadherin by NF–YAs and NF–YAl confers diverse biological properties to CRC cells, in terms of growth and migration. NF-YAl^{high} levels enhance metastatic dissemination of CRC cells, characterize aggressive tumors and predict poor overall survival of CRC patients. Created with BioRender.com.

Declaration of competing interest

The authors declare that they have no known competing financial interests or personal relationships that could have appeared to influence the work reported in this paper.

Acknowledgements

The research leading to these results has received funding from AIRC (Fondazione Italiana per la Ricerca sul Cancro) under IG 2018 – I.D. 21323 project – P.I. Carol Imbriano and Finanziamento FAR_DIP2021 to Carol Imbriano. The project is funded under the National Recovery and Resilience Plan (NRRP), Mission 4 Component 2 Investment 1.4 - MUR public notice n. 3138/2021 as modified by DD 3175/2021 funded by the European Union – NextGenerationEU, CN_3: National Center for Gene Therapy and Drugs based on RNA Technology Spoke 2 - Cancer", project code CN 00000041, and NRRP, Mission 4 Component 2 Investment 1.3 - MUR public notice n. 341 of 03.15.2022 funded by the European Union – NextGenerationEU, Creation of "Partnerships extended to universities, research centres, companies for the financing of basic research projects", HEAL ITALIA Spoke 3, project code PE00000019.

Appendix A. Supplementary data

Supplementary data to this article can be found online at https://doi.org/10.1016/j.canlet.2023.216262.

List of abbreviations

NF–Y	Nuclear Factor Y
CRC	Colorectal Cancer
EMT	Epithelial to Mesenchymal Transition
COAD	Colon Adenocarcinoma
ECM	Extracellular Matrix
MTS	Multicellular Tumor Spheroid
CTC	Circulating Tumor Cell
ASO	antisense oligonucleotide

References

[1] D. Dolfini, R. Gatta, R. Mantovani, NF-Y and the transcriptional activation of CCAAT promoters, Crit. Rev. Biochem. Mol. Biol. 47 (2012) 29–49, https://doi.org/10.3109/10409238.2011.628970.
[2] I. Abnizova, K. Walter, R. Te Boekhorst, G. Elgar, W.R. Gilks, Statistical information characterization of conserved non-coding elements in vertebrates, J. Bioinf. Comput. Biol. 5 (2007) 533–547, https://doi.org/10.1142/s0219720007002898.
[3] R. Elkon, C. Linhart, R. Sharan, R. Shamir, Y. Shiloh, Genome-wide in silico identification of transcriptional regulators controlling the cell cycle in human cells, Genome Res. 13 (2003) 773–780, https://doi.org/10.1101/gr.947203.
[4] H. Goodarzi, O. Elemento, S. Tavazoie, Revealing global regulatory perturbations across human cancers, Mol. Cell. 36 (2009) 900–911, https://doi.org/10.1016/j.molcel.2009.11.016.
[5] A. Häkkinen, S. Healy, H.T. Jacobs, A.S. Ribeiro, Genome wide study of NF-Y type CCAAT boxes in unidirectional and bidirectional promoters in human and mouse, J. Theor. Biol. 281 (2011) 74–83, https://doi.org/10.1016/j.jtbi.2011.04.027.
[6] A. Gurtner, I. Manni, G. Piaggio, NF-Y in cancer: impact on cell transformation of a gene essential for proliferation, Biochimica et Biophysica Acta (BBA) - Gene Regulatory Mechanisms 1860 (2017) 604–616, https://doi.org/10.1016/J.BBAGRM.2016.12.005.
[7] P. Benatti, M.L. Chiaramonte, M. Lorenzo, J.A. Hartley, D. Hochhauser, N. Gnesutta, R. Mantovani, C. Imbriano, D. Dolfini, NF-Y activates genes of metabolic pathways altered in cancer cells, Oncotarget 7 (2016) 1633–1650, https://doi.org/10.18632/oncotarget.6453.
[8] L.-Y. Bie, D. Li, Y. Mu, S. Wang, B.-B. Chen, H.-F. Lyu, L.-L. Han, C.-Y. Nie, C.-C. Yang, L. Wang, C.-C. Ren, W.-J. Zhang, P. Guo, F. Shi, Q.-X. Fan, L.-X. Wang, X.-B. Chen, S.-X. Luo, Analysis of cyclin E co-expression genes reveals nuclear

transcription factor Y subunit alpha is an oncogene in gastric cancer, Chronic Dis Transl Med 5 (2019) 44–52, https://doi.org/10.1016/j.cdtm.2018.07.003.
[9] E. Bezzecchi, M. Ronzio, D. Dolfini, R. Mantovani, NF-YA overexpression in lung cancer: LUSC, Genes 10 (2019), https://doi.org/10.3390/genes10110937.
[10] E. Bezzecchi, M. Ronzio, V. Semeghini, V. Andrioletti, R. Mantovani, D. Dolfini, NF-YA overexpression in lung cancer: luad, Genes 11 (2020) 198, https://doi.org/10.3390/genes11020198.
[11] A. Garipov, H. Li, B.G. Bitler, R.J. Thapa, S. Balachandran, R. Zhang, NF-YA underlies EZH2 upregulation and is essential for proliferation of human epithelial ovarian cancer cells, Mol. Cancer Res. 11 (2013) 360, https://doi.org/10.1158/1541-7786.MCR-12-0661.
[12] J. Guo, L.M. Kong, A.F. Peng, X.H. Long, Y. Zhou, Y. Shu, Transcription factor NF-YA promotes a malignant phenotype by upregulating fatty acid synthase expression, Mol. Med. Rep. 14 (2016) 5007–5014, https://doi.org/10.3892/mmr.2016.5897.
[13] D. Dolfini, V. Andrioletti, R. Mantovani, Overexpression and alternative splicing of NF-YA in breast cancer, Sci. Rep. 9 (2019) 12955, https://doi.org/10.1038/s41598-019-49297-5, 12955.
[14] S. Belluti, V. Semeghini, G. Rigillo, M. Ronzio, D. Benati, F. Torricelli, L. Reggiani Bonetti, G. Carnevale, G. Grisendi, A. Ciarrocchi, M. Dominici, A. Recchia, D. Dolfini, C. Imbriano, Alternative splicing of NF-YA promotes prostate cancer aggressiveness and represents a new molecular marker for clinical stratification of patients, J. Exp. Clin. Cancer Res. 40 (2021) 362, https://doi.org/10.1186/s13046-021-02166-4.
[15] H. Cui, M. Zhang, Y. Wang, Y. Wang, NF-YC in glioma cell proliferation and tumor growth and its role as an independent predictor of patient survival, Neurosci. Lett. 631 (2016) 40–49, https://doi.org/10.1016/J.NEULET.2016.08.003.
[16] Y. Tong, D. Merino, B. Nimmervoll, K. Gupta, Y.D. Wang, D. Finkelstein, J. Dalton, D.W. Ellison, X. Ma, J. Zhang, D. Malkin, R.J. Gilbertson, Cross-species genomics identifies TAF12, NFYC, and RAD54L as choroid plexus carcinoma oncogenes, Cancer Cell 27 (2015) 712–727, https://doi.org/10.1016/j.ccell.2015.04.005.
[17] S. Belluti, G. Rigillo, C. Imbriano, Transcription factors in cancer: when alternative splicing determines opposite cell fates, Cells 9 (2020) 760, https://doi.org/10.3390/cells9030760.
[18] L. Cicchillitti, G. Corrado, M. Carosi, M.E. Dabrowska, R. Loria, R. Falcioni, G. Cutillo, G. Piaggio, E. Vizza, Prognostic role of NF-YA splicing isoforms and Lamin A status in low grade endometrial cancer, Oncotarget 8 (2017) 7935–7945, https://doi.org/10.18632/oncotarget.13854.
[19] C.W. James D. Brierley, Mary K. Gospodarowicz, TNM Classification of Malignant Tumours, eighth ed., Wiley, Wiley-Blackwell, 2017.
[20] R. Amirkhah, H. Naderi-Meshkin, J. Shah, P. Dunne, U. Schmitz, The intricate interplay between epigenetic events, alternative splicing and noncoding RNA deregulation in colorectal cancer, Cells 8 (2019) 929, https://doi.org/10.3390/cells8080929.
[21] D.M. Muzny, M.N. Bainbridge, K. Chang, H.H. Dinh, J.A. Drummond, G. Fowler, C. L. Kovar, L.R. Lewis, M.B. Morgan, I.F. Newsham, J.G. Reid, J. Santibanez, E. Shinbrot, L.R. Trevino, Y.Q. Wu, M. Wang, P. Gunaratne, L.A. Donehower, C. J. Creighton, D.A. Wheeler, R.A. Gibbs, M.S. Lawrence, D. Voet, R. Jing, K. Cibulskis, A. Sivachenko, P. Stojanov, A. McKenna, E.S. Lander, S. Gabriel, L. Ding, R.S. Fulton, D.C. Koboldt, T. Wylie, J. Walker, D.J. Dooling, L. Fulton, K. D. Delehaunty, C.C. Fronick, R. Demeter, E.R. Mardis, R.K. Wilson, A. Chu, H.J. E. Chun, A.J. Mungall, E. Pleasance, A. Gordon Robertson, D. Stoll, M. Balasundaram, I. Birol, Y.S.N. Butterfield, E. Chuah, R.J.N. Coope, N. Dhalla, R. Guin, C. Hirst, M. Hirst, R.A. Holt, D. Lee, H.I. Li, M. Mayo, R.A. Moore, J. E. Schein, J.R. Slobodan, A. Tam, N. Thiessen, R. Varhol, T. Zeng, Y. Zhao, S.J. M. Jones, M.A. Marra, A.J. Bass, A.H. Ramos, G. Saksena, A.D. Cherniack, S. E. Schumacher, B. Tabak, S.L. Carter, N.H. Pho, H. Nguyen, R.C. Onofrio, A. Crenshaw, K. Ardlie, R. Beroukhim, W. Winckler, M. Meyerson, A. Protopopov, A. Hadjipanayis, E. Lee, R. Xi, L. Yang, X. Ren, N. Sathiamoorthy, P.C. Chen, P. Haseley, Y. Xiao, S. Lee, J. Seidman, L. Chin, P.J. Park, R. Kucherlapati, J. Todd Auman, K.A. Hoadley, Y. Du, M.D. Wilkerson, Y. Shi, C. Liquori, S. Meng, L. Li, Y. J. Turman, M.D. Topal, D. Tan, S. Waring, E. Buda, J. Walsh, C.D. Jones, P. A. Mieczkowski, D. Singh, J. Wu, A. Gulabani, P. Dolina, T. Bodenheimer, A. P. Hoyle, J.V. Simons, M. Soloway, L.E. Mose, S.R. Jefferys, S. Balu, B.D. O'Connor, J.F. Prins, D.Y. Chiang, D. Neil Hayes, C.M. Perou, T. Hinoue, D.J. Weisenberger, D. T. Maglinte, F. Pan, B.P. Berman, D.J. Van Den Berg, H. Shen, T. Triche, S. B. Baylin, P.W. Laird, G. Getz, M. Noble, D. Voat, N. Gehlenborg, D. Dicara, J. Zhang, H. Zhang, C.J. Wu, S.Y. Liu, S. Shukla, L. Zhou, P. Lin, R.W. Park, M. D. Nazaire, J. Robinson, H. Thorvaldsdottir, J. Mesirov, V. Thorsson, S. M. Reynolds, B. Bernard, R. Kreisberg, J. Lin, L. Iype, R. Bressler, T. Erkkilä, M. Gundapuneni, Y. Liu, A. Norberg, T. Robinson, D. Yang, W. Zhang, I. Shmulevich, J.J. De Ronde, N. Schultz, E. Cerami, G. Ciriello, A.P. Goldberg, B. Gross, A. Jacobsen, J. Gao, B. Kaczkowski, R. Sinha, B. Arman Aksoy, Y. Antipin, B. Reva, R. Shen, B.S. Taylor, M. Ladanyi, C. Sander, R. Akbani, N. Zhang, B. M. Broom, T. Casasent, A. Unruh, C. Wakefield, S.R. Hamilton, R. Craig Cason, K. A. Baggerly, J.N. Weinstein, D. Haussler, C.C. Benz, J.M. Stuart, S.C. Benz, J. Zachary Sanborn, C.J. Vaske, J. Zhu, C. Szeto, G.K. Scott, C. Yau, S. Ng, T. Goldstein, K. Ellrott, E. Collisson, A.E. Cozen, D. Zerbino, C. Wilks, B. Craft, P. Spellman, R. Penny, T. Shelton, M. Hatfield, S. Morris, P. Yena, C. Shelton, M. Sherman, J. Paulauskis, J.M. Gastier-Foster, J. Bowen, N.C. Ramirez, A. Black, R. Pyatt, L. Wise, P. White, M. Bertagnolli, J. Brown, T.A. Chan, G.C. Chu, C. Czerwinski, F. Denstman, R. Dhir, A. Dörner, C.S. Fuchs, J.G. Guillem, M. Iacocca, H. Juhl, A. Kaufman, B.K. Iii, X. Van Le, M.C. Mariano, E.N. Medina, M. Meyers, G.M. Nash, P.B. Paty, N. Petrelli, B. Rabeno, W.G. Richards, D. Solit, P. Swanson, L. Temple, J.E. Tepper, R. Thorp, E. Vakiani, M.R. Weiser, J.E. Willis, G. Witkin, Z. Zeng, M.J. Zinner, C. Zornig, M.A. Jensen, R. Sfeir, A.B. Kahn, A. L. Chu, P. Kothiyal, Z. Wang, E.E. Snyder, J. Pontius, T.D. Pihl, B. Ayala, M. Backus, J. Walton, J. Whitmore, J. Baboud, D.L. Berton, M.C. Nicholls, D. Srinivasan, R. Raman, S. Girshik, P.A. Kigonya, S. Alonso, R.N. Sanbhadti, S.P. Barletta, J. M. Greene, D.A. Pot, K.R.M. Shaw, L.A.L. Dillon, K. Buetow, T. Davidsen, J. A. Demchok, G. Eley, M. Ferguson, P. Fielding, C. Schaefer, M. Sheth, L. Yang, M. S. Guyer, B.A. Ozenberger, J.D. Palchik, J. Peterson, H.J. Sofia, E. Thomson, Comprehensive molecular characterization of human colon and rectal cancer, Nature 487 (2012) 330–337, https://doi.org/10.1038/nature11252.
[22] B. Perez Villamil, A. Romera Lopez, S. Hernandez Prieto, G. Lopez Campos, A. Calles, J.A. Lopez Asenjo, J. Sanz Ortega, C. Fernandez Perez, J. Sastre, R. Alfonso, T. Caldes, F. Martin Sanchez, E. Diaz Rubio, Colon cancer molecular subtypes identified by expression profiling and associated to stroma, mucinous type and different clinical behavior, BMC Cancer 12 (2012) 260, https://doi.org/10.1186/1471-2407-12-260.
[23] J. Guinney, R. Dienstmann, X. Wang, A. De Reyniès, A. Schlicker, C. Soneson, L. Marisa, P. Roepman, G. Nyamundanda, P. Angelino, B.M. Bot, J.S. Morris, I. M. Simon, S. Gerster, E. Fessler, F. De Sousa E Melo, E. Missiaglia, H. Ramay, D. Barras, K. Homicsko, D. Maru, G.C. Manyam, B. Broom, V. Boige, B. Perez-Villamil, T. Laderas, R. Salazar, J.W. Gray, D. Hanahan, J. Tabernero, R. Bernards, S.H. Friend, P. Laurent-Puig, J.P. Medema, A. Sadanandam, L. Wessels, M. Delorenzi, S. Kopetz, L. Vermeulen, S. Tejpar, The consensus molecular subtypes of colorectal cancer, Nat. Med. 21 (2015) 1350–1356, https://doi.org/10.1038/nm.3967.
[24] C. Bonnans, J. Chou, Z. Werb, Remodelling the extracellular matrix in development and disease, Nat. Rev. Mol. Cell Biol. 15 (2014) 786–801, https://doi.org/10.1038/nrm3904.
[25] P. Lu, V.M. Weaver, Z. Werb, The extracellular matrix: a dynamic niche in cancer progression, JCB (J. Cell Biol.) 196 (2012) 395–406, https://doi.org/10.1083/jcb.201102147.
[26] M.J. Goldman, B. Craft, M. Hastie, K. Repečka, F. McDade, A. Kamath, A. Banerjee, Y. Luo, D. Rogers, A.N. Brooks, J. Zhu, D. Haussler, Visualizing and interpreting cancer genomics data via the Xena platform, Nat. Biotechnol. 38 (2020) 675–678, https://doi.org/10.1038/s41587-020-0546-8.
[27] L. Mi, H. W, A. S, Moderated estimation of fold change and dispersion for RNA-seq data with DESeq2, Genome Biol. 15 (2014), https://doi.org/10.1186/S13059-014-0550-8.
[28] F. Gao, W. Wang, M. Tan, L. Zhu, Y. Zhang, E. Fessler, L. Vermeulen, X. Wang, DeepCC: a novel deep learning-based framework for cancer molecular subtype classification, Oncogenesis 8 (2019) 1–12, https://doi.org/10.1038/s41389-019-0157-8.
[29] B. Langmead, S.L. Salzberg, Fast gapped-read alignment with Bowtie 2, Nat. Methods 9 (2012) 357–359, https://doi.org/10.1038/nmeth.1923.
[30] B. Li, C.N. Dewey, RSEM: accurate transcript quantification from RNA-Seq data with or without a reference genome, BMC Bioinf. 12 (2011) 323, https://doi.org/10.1186/1471-2105-12-323.
[31] G. Ragazzini, A. Mescola, L. Corsi, A. Alessandrini, Fabrication of a Low-Cost On-Stage Cell Incubator with Full Automation, 2018, pp. 165–173, https://doi.org/10.1080/00219266.2018.1451772, 10.1080/00219266.2018.1451772. 53.
[32] J. Schindelin, I. Arganda-Carreras, E. Frise, V. Kaynig, M. Longair, T. Pietzsch, S. Preibisch, C. Rueden, S. Saalfeld, B. Schmid, J.Y. Tinevez, D.J. White, V. Hartenstein, K. Eliceiri, P. Tomancak, A. Cardona, Fiji - an Open Source platform for biological image analysis, Nat. Methods 9 (2012) 676–682, https://doi.org/10.1038/NMETH.2019.
[33] A. Suarez-Arnedo, F.T. Figueroa, C. Clavijo, P. Arbeláez, J.C. Cruz, C. Muñoz-Camargo, An image J plugin for the high throughput image analysis of in vitro scratch wound healing assays, PLoS One 15 (2020), e0232565, https://doi.org/10.1371/JOURNAL.PONE.0232565.
[34] G. Rigillo, V. Basile, S. Belluti, M. Ronzio, E. Sauta, A. Ciarrocchi, L. Latella, M. Saclier, S. Molinari, A. Vallarola, G. Messina, R. Mantovani, D. Dolfini, C. Imbriano, The transcription factor NF-Y participates to stem cell fate decision and regeneration in adult skeletal muscle, Nat. Commun. 12 (2021) 1–17, https://doi.org/10.1038/s41467-021-26293-w.
[35] P. Benatti, V. Basile, D. Dolfini, S. Belluti, M. Tomei, C. Imbriano, NF-Y loss triggers p53 stabilization and apoptosis in HPV18-positive cells by affecting E6 transcription, Oncotarget 7 (2016), https://doi.org/10.18632/oncotarget.9974.
[36] M. Mazda, K. Nishi, Y. Naito, K. Ui-Tei, E-cadherin is transcriptionally activated via suppression of ZEB1 transcriptional repressor by small RNA-mediated gene silencing, PLoS One 6 (2011), 28688, https://doi.org/10.1371/journal.pone.0028688.
[37] C. Imbriano, A. Gurtner, F. Cocchiarella, S. Di Agostino, V. Basile, M. Gostissa, M. Dobbelstein, G. Del Sal, G. Piaggio, R. Mantovani, Direct p53 transcriptional repression: in vivo analysis of CCAAT-containing G2/M promoters, Mol. Cell Biol. 25 (2005) 3737–3751, https://doi.org/10.1128/MCB.25.9.3737-3751.2005.
[38] S. Belluti, V. Semeghini, V. Basile, G. Rigillo, V. Salsi, F. Genovese, D. Dolfini, C. Imbriano, An autoregulatory loop controls the expression of the transcription factor NF-Y, Biochim Biophys Acta Gene Regul Mech 1861 (2018) 509–518, https://doi.org/10.1016/j.bbagrm.2018.02.008.
[39] C.B. Kimmel, W.W. Ballard, S.R. Kimmel, B. Ullmann, T.F. Schilling, Stages of embryonic development of the zebrafish, Dev. Dynam. 203 (1995) 253–310, https://doi.org/10.1002/AJA.1002030302.
[40] E. Bezzecchi, M. Ronzio, R. Mantovani, D. Dolfini, NF-Y overexpression in liver hepatocellular carcinoma (HCC), Int. J. Mol. Sci. 21 (2020) 1–16, https://doi.org/10.3390/ijms21239157.
[41] V. Basile, F. Baruffaldi, D. Dolfini, S. Belluti, P. Benatti, L. Ricci, V. Artusi, E. Tagliafico, R. Mantovani, S. Molinari, C. Imbriano, NF-YA splice variants have

different roles on muscle differentiation, Biochim Biophys Acta Gene Regul Mech 1859 (2016) 627–638, https://doi.org/10.1016/j.bbagrm.2016.02.011.
[42] H. Hatzikirou, D. Basanta, M. Simon, K. Schaller, A. Deutsch, 'Go or Grow': the key to the emergence of invasion in tumour progression? Math. Med. Biol. 29 (2012) 49–65, https://doi.org/10.1093/IMAMMB/DQQ011.
[43] J. shun Wu, J. Jiang, B. jun Chen, K. Wang, Y. ling Tang, X. hua Liang, Plasticity of cancer cell invasion: patterns and mechanisms, Transl Oncol 14 (2021), https://doi.org/10.1016/J.TRANON.2020.100899.
[44] V. Graziani, I. Rodriguez-Hernandez, O. Maiques, V. Sanz-Moreno, The amoeboid state as part of the epithelial-to-mesenchymal transition programme, Trends Cell Biol. 32 (2022) 228–242, https://doi.org/10.1016/J.TCB.2021.10.004.
[45] J.T. Parsons, A.R. Horwitz, M.A. Schwartz, Cell adhesion: integrating cytoskeletal dynamics and cellular tension, Nat. Rev. Mol. Cell Biol. 11 (2010) 633–643, https://doi.org/10.1038/nrm2957, 2010 11:9.
[46] W. Xu, Z. Yang, N. Lu, A new role for the PI3K/Akt signaling pathway in the epithelial-mesenchymal transition, Cell Adhes. Migrat. 9 (2015) 317–324, https://doi.org/10.1080/19336918.2015.1016686.
[47] L. Li, R. Hartley, B. Reiss, Y. Sun, J. Pu, D. Wu, F. Lin, T. Hoang, S. Yamada, J. Jiang, M. Zhao, E-cadherin plays an essential role in collective directional migration of large epithelial sheets, Cell. Mol. Life Sci. 69 (2012) 2779–2789, https://doi.org/10.1007/S00018-012-0951-3, 2012 69:16.
[48] R. Mantovani, X.Y. Li, U. Pessara, R. Hooft Van Huisjduijnen, C. Benoist, D. Mathis, Dominant negative analogs of NF-YA, J. Biol. Chem. 269 (1994) 20340–20346, https://doi.org/10.1016/S0021-9258(17)31997-X.
[49] C. Cicchini, I. Laudadio, F. Citarella, M. Corazzari, C. Steindler, A. Conigliaro, A. Fantoni, L. Amicone, M. Tripodi, TGFβ-induced EMT requires focal adhesion kinase (FAK) signaling, Exp. Cell Res. 314 (2008) 143–152, https://doi.org/10.1016/J.YEXCR.2007.09.005.
[50] Y. Fujita, G. Krause, M. Scheffner, D. Zechner, H.E.M. Leddy, J. Behrens, T. Sommer, W. Birchmeier, Hakai, a c-Cbl-like protein, ubiquitinates and induces endocytosis of the E-cadherin complex, Nat. Cell Biol. 4 (2002) 222–231, https://doi.org/10.1038/ncb758, 2002 4:3.
[51] T. Brabletz, To differentiate or not — routes towards metastasis, Nat. Rev. Cancer 12 (2012) 425–436, https://doi.org/10.1038/nrc3265, 2012 12:6.
[52] X.-X. Jie, X.-Y. Zhang, C.-J. Xu, Epithelial-to-mesenchymal transition, circulating tumor cells and cancer metastasis: mechanisms and clinical applications, Oncotarget 8 (2017) 81558–81571.
[53] W. Lu, Y. Kang, Epithelial-mesenchymal plasticity in cancer progression and metastasis, Dev. Cell 49 (2019) 361–374, https://doi.org/10.1016/J.DEVCEL.2019.04.010.
[54] D. Sinha, P. Saha, A. Samanta, A. Bishayee, Emerging concepts of hybrid epithelial-to-mesenchymal transition in cancer progression, Biomolecules 10 (11) (2020 Nov 16) 1561, https://doi.org/10.3390/biom10111561.
[55] F. Van Roy, G. Berx, The cell-cell adhesion molecule E-cadherin, Cell. Mol. Life Sci. 65 (2008) 3756–3788, https://doi.org/10.1007/S00018-008-8281-1.
[56] Y. Elisha, V. Kalchenko, Y. Kuznetsov, B. Geiger, Dual role of E-cadherin in the regulation of invasive collective migration of mammary carcinoma cells OPEN, Sci. Rep. 8 (2018) 4986, https://doi.org/10.1038/s41598-018-22940-3.
[57] A. Haeger, K. Wolf, M.M. Zegers, P. Friedl, Collective cell migration: guidance principles and hierarchies, Trends Cell Biol. 25 (2015) 556–566, https://doi.org/10.1016/J.TCB.2015.06.003.
[58] S. Hee Park, S. Ra Lee, B. Chul Kim, E. Ah Cho, S.P. Patel, H.-B. Kang, E. A. Sausville, O. Nakanishi, J.B. Trepel, B. Ick Lee, S.-J. Kim, Transcriptional regulation of the transforming growth factor Î2 type II receptor gene by histone acetyltransferase and deacetylase is mediated by NF-Y in human breast cancer cells, J. Biol. Chem. 277 (2002) 5168–5174, https://doi.org/10.1074/jbc.M106451200.
[59] Y. Peng, N. Jahroudi, The NFY transcription factor functions as a repressor and activator of the von Willebrand factor promoter, Blood 99 (2002) 2408–2417, https://doi.org/10.1182/BLOOD.V99.7.2408.
[60] X. Zhu, Y. Wang, W. Pi, H. Liu, A. Wickrema, D. Tuan, NF-Y recruits both transcription activator and repressor to modulate tissue- and developmental stage-specific expression of human γ- globin gene, PLoS One 7 (2012), e47175, https://doi.org/10.1371/JOURNAL.PONE.0047175.
[61] Q.L. Liu, M. Luo, C. Huang, H.N. Chen, Z.G. Zhou, Epigenetic regulation of epithelial to mesenchymal transition in the cancer metastatic cascade: implications for cancer therapy, Front. Oncol. 11 (2021), https://doi.org/10.3389/FONC.2021.657546.
[62] A. Bera, S.M. Lewis, Regulation of Epithelial-to-Mesenchymal Transition by Alternative Translation Initiation Mechanisms and Its Implications for Cancer Metastasis, Int. J. Mol. Sci. 21 (11) (2020) 4075, https://doi.org/10.3390/ijms21114075.
[63] I.A. Voutsadakis, The ubiquitin–proteasome system and signal transduction pathways regulating Epithelial Mesenchymal transition of cancer, J. Biomed. Sci. 19 (2012) 1–13, https://doi.org/10.1186/1423-0127-19-67, 2012 19:1.